Earthquakes and Heavy Rainfall Influence on Aquifer Properties: A New Coupled Earth and Barometric Tidal Response Model in a Confined Bi-Layer Aquifer

A. Thomas, J. Fortin, B. Vittecoq, S. Violette

Water Resources Research

RESEARCH ARTICLE
10.1029/2022WR033367

Earthquakes and Heavy Rainfall Influence on Aquifer Properties: A New Coupled Earth and Barometric Tidal Response Model in a Confined Bi-Layer Aquifer

A. Thomas[1], J. Fortin[1], B. Vittecoq[2], and S. Violette[1,3]

[1]Laboratoire de Géologie, Ecole Normale Supérieure - PSL Research University, CNRS, Paris, France, [2]BRGM, Fort-de-France, Martinique, [3]Sorbonne University, UFR.918, Paris, France

Key Points:

- A model for the tidal response of bi-layer aquifers was developed, focusing on pressure diffusion and exchange between two confined layers
- Using 14 years of hourly piezometric data, the temporal evolution of aquifer diffusivity was inferred and confirmed independently by pumping tests
- The change of permeability is shown to be due to earthquakes, extreme rainfall events and aquifer withdrawals in upstream borehole

Supporting Information:

Supporting Information may be found in the online version of this article.

Correspondence to:

A. Thomas,
augustin.thomas@ens.fr

Citation:

Thomas, A., Fortin, J., Vittecoq, B., & Violette, S. (2023). Earthquakes and heavy rainfall influence on aquifer properties: A new coupled Earth and barometric tidal response model in a confined bi-layer aquifer. *Water Resources Research*, *59*, e2022WR033367. https://doi.org/10.1029/2022WR033367

Received 4 AUG 2022
Accepted 6 MAR 2023

Abstract Among the impacts of earthquakes on aquifers, permeability change is one of the most challenging to quantify, since techniques to measure permeability evolution are scarce. The study of tidal response of boreholes is one of the most promising, yet complex to use in practice. We used 14 years of piezometric level measurements and two concurrent source signals, earth tidal strain and barometric pressure, for which we separated the respective contribution in a state-of-the-art tidal analysis. We developed a new general analytical hydrogeological model, based on geological observations of a confined bi-layer aquifer. It is able to match combined observations of earth and barometric tide phase lags which could not be explained by existing models. We demonstrate that its relative complexity can be overcome thanks to the results of tidal analysis, yielding a simpler model adapted to the Fond Lahaye site of the Martinique Island. The resulting evolution of diffusivity and loading efficiency, was validated independently with several pumping tests occurring all along the studied period. The transient diffusivity increases and decreases indicate which earthquakes impacted the aquifer, enabling to establish an empirical magnitude-distance relationship criterion. This criterion confirms the suspected dependence on dynamic stresses, which decrease as the square of the hypocentral distance. Additionally, we investigate two other factors of diffusivity changes: heavy rainfall events and aquifer withdrawals, which demonstrates the sensitivity of volcanic aquifers properties to environmental and anthropogenic influence.

1. Introduction

Piezometric level response to periodic forcings, like solid earth tide strain, barometric loading or oceanic tide loading, is a useful alternative way to characterize aquifer properties. It was first spread as a tool for aquifer characterization 34 years ago with the model of Hsieh et al. (1987). It was promising in the sense it only needs classical monitoring data (hourly water level) and no expensive field work like a pumping test. Yet its usage is still far from its potential as expressed in the review of McMillan et al. (2019). On the one hand, the pumping test literature, relatively old, covers a wide variety of aquifer geometries and boundary conditions, including, without comprehensiveness, models for confined radial aquifer (Theis, 1935), leaky aquifers (Hantush & Jacob, 1955), double porosity aquifers (Warren & Root, 1963), unconfined aquifer (Neuman, 1972), spatially heterogeneous aquifers with the general radial flow model (Barker, 1988). Research is still ongoing namely on numerical modeling to complexify the possible responses. On the other hand, literature on periodic responses only recently represented a decent variety of aquifer geometry, starting from Roeloffs (1996) and Rojstaczer (1988) for unconfined aquifers, to Wang et al. (2018) for leaky aquifers. Research on this topic now faces the challenge of proposing a comprehensive view and practical guidelines, like did in its time the useful tutorial of Doan et al. (2008). Now the two major and somewhat opposing pitfalls scientists face are the following. The first one is that the existing models are based on strong hypotheses (perfect confinement for Hsieh et al. (1987), negligible storage in the aquitard in Wang et al. (2018),) which of course are not in general met. There is still room for a more general derivation of analytical models, like what Odling et al. (2015) did in the case of the model of Rojstaczer (1988), precising the low frequency behavior which was improperly predicted. The second pitfall, opposing to the first, is that we need to remain as simple as possible, and keep in mind the mathematical limitations of modeling inversion: from n observed variables, we can invert at best n parameters. In that sense, periodic response problems are nearly always over-parametrized, since observations are often limited to phase and amplitude response at one or two frequencies, while hydrodynamic and poroelastic parameters (hydraulic conductivity, storativity, etc.), grow numerous with the complexity of the models. In this paper, we do not claim to give the comprehensive view we

call for, but go one step toward and present a case study where we try to methodically avoid the two previously identified pitfalls. Building on the geological knowledge of the field (Section 2.1), we build a new model adapted to our aquifer geometry, without a priori hypotheses on the parameters (Sections 4.1–4.3). To better the odds of being able to invert the model, we calculated the tidal responses of the two significant signal sources, and disentangled their contributions (Section 3), like recommended in McMillan et al. (2019), and implemented in Valois et al. (2022). As a secondary step only, we use all of this information to constrain and invert the model (Sections 4.5 and 4.6). Thanks to a validation with several pumping tests (Section 4.7), we can confidently discuss the evolution of the inverted parameters and the different phenomena at stakes (Section 5.1). Indeed, a major benefit of the method is to provide the evolution of hydrodynamic parameters evolution across time. Thus, it was frequently implemented to study the response of aquifers to earthquakes (Elkhoury et al., 2006; Shi et al., 2019; Sun et al., 2020; Wang et al., 2016; Zhang, 2019), which where proven to have numerous impacts on aquifer systems, from water level oscillations, water level coseismic drop or rise (Brodsky et al., 2003), new springs appearance or increase in stream discharges (Wang & Manga, 2015), mud volcano eruptions (Manga & Wang, 2015), to what interest us particularly here: permeability changes (Elkhoury et al., 2006; Ingebritsen & Manga, 2019; Rojstaczer et al., 1995). Several processes have been proposed in the literature to explain permeability changes, including effective pressure changes (Muir-Wood & King, 1993; E. Roeloffs et al., 2003), clogging-unclogging of fractures (Barbosa et al., 2019; Brodsky et al., 2003; Candela, 2014), opening of new fractures (Wang et al., 2016; Xue et al., 2013) or liquefaction/consolidation (Manga, 2001; Montgomery & Manga, 2003). In the far field, these changes, caused by dynamic stresses are often transient (Manga et al., 2012), and the empirical relationships linking the maximum distance at which an earthquake of given magnitude can affect the crust depend on the phenomena. Roeloffs (1998) proposed a relationship for constant pore pressure changes, Wang and Manga (2010) proposed the seismic energy density as a general metric. Here we show that dynamic stresses may be more relevant in the far field, since they decay as the square of the distance for surface waves (Section 5.1). Finally the time-dependent diffusivity inverted also showcases a response to heavy tropical rainfall events like observed in another watershed in Martinique (Vittecoq et al., 2020) as well as to aquifer withdrawals, illustrating how sensitive to environmental and anthropogenic influence fractured aquifers properties can be.

2. The Martinique Fond Lahaye Aquifer

2.1. Geological Context

Martinique is a volcanic island of the Lesser Antilles archipelago, resulting from the subduction of the Atlantic lithosphere bellow the Caribbean plate (Figure 1). It is the largest volcanic island of the archipelago (1,080 km^2), with a volcanic activity, mainly andesitic, for at least 25 Ma (Westercamp et al., 1990). The resulting relief is mountainous in the north (highest and youngest volcano, Montagne Pelée, at 1,397 m) and gentler in the south with highest relief at 504 m. Climate in Martinique is humid tropical, with a rainy season between July and November with precipitation brought by trade winds reaching 5,000–6,500 mm $\cdot$ yr^{-1} at the northern summits and between 1,200 and 1,500 mm yr^{-1} in the south. Temperatures vary between 18 and 32°C at Fort-de-France (Vittecoq et al., 2019). Over the period 2007–2019, 128 earthquakes were felt in Martinique (Figure 1) and reported by the Volcanological and Seismological Observatory of Martinique (OVSM-IPGP) (min magnitude 2.1, median 4.2 and max 7.4). The Fond Lahaye borehole is situated in a valley situated on the west coast of the island, 2 km from the sea, at an elevation of 76.3 m amsl (Figure 1). The geological formations in the valley are 5.5-2.2 Ma fractured andesite lava flows topped by conglomerates, debris, block and alluvium from the dismantling of the upper volcanic edifice (Carbet volcanic complex) (Vittecoq et al., 2019; Westercamp et al., 1990). The aquifer corresponds to the fractured andesite (30–62 m below surface), which upper part has been altered up to residual andesite blocks in a clay matrix which act as a barrier for fluid flow (Figure 2). The conglomerates and alluvium on top (2–22 m below surface) are dry: no water inflow was observed during drilling, this is also confirmed by resistivity measurements as shown by the resistivity log on Figure 2 (Vittecoq & Brugeron, 2008). The borehole is 62 m deep, and opened to the aquifer between −22 and −62 m. The drilling radius r_w is 194 mm and the casing radius r_c 125 mm. The water level, which is above the aquifer top, confirms the confined type of the aquifer.

2.2. Data Presentation

Data consists of 14 years of hourly piezometric level records, starting from February 2008 (Figure 3a). Two sensors have been used both with millimetric resolution. OTT Thalimedes from 2005 to 2014, a float operated

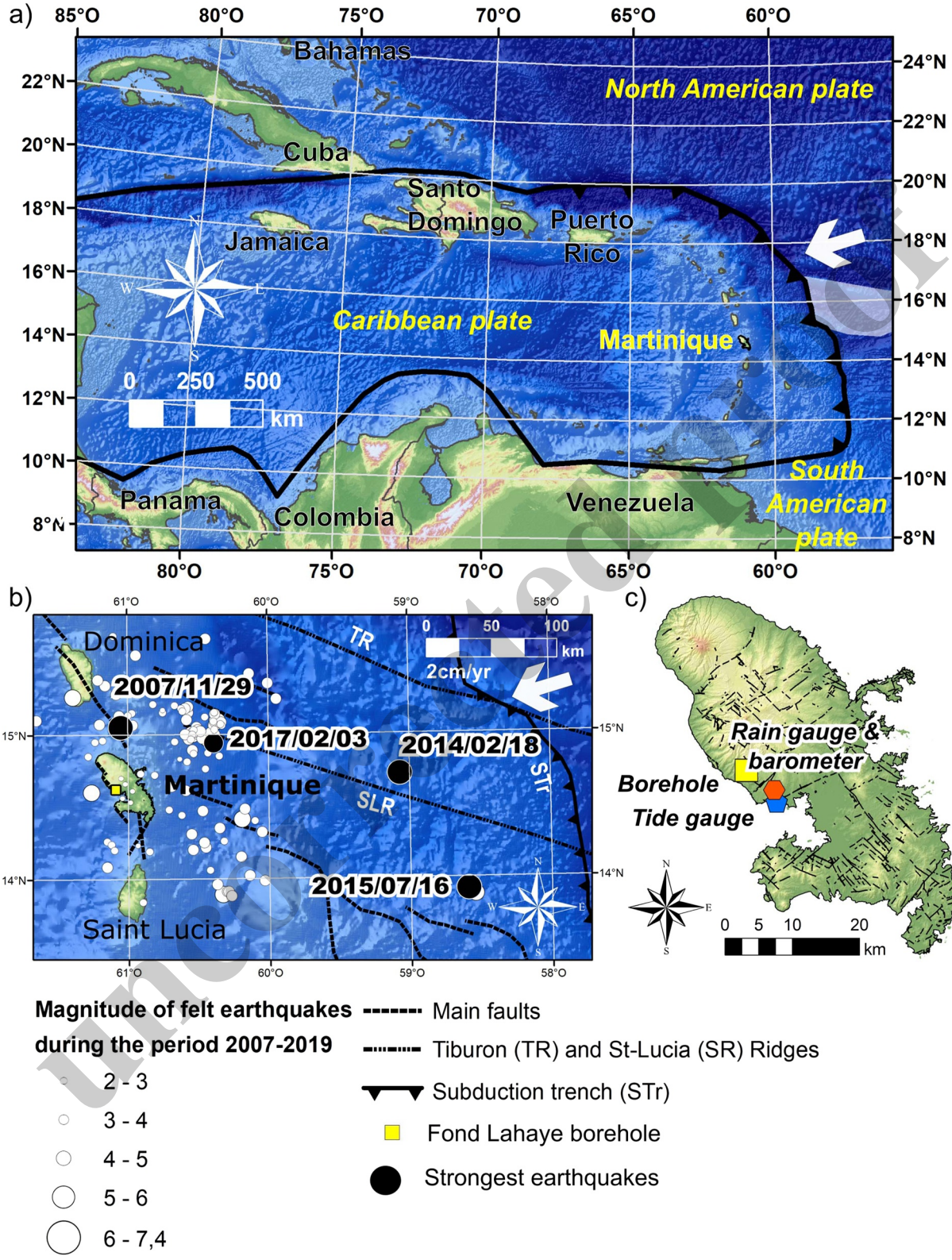

Figure 1.

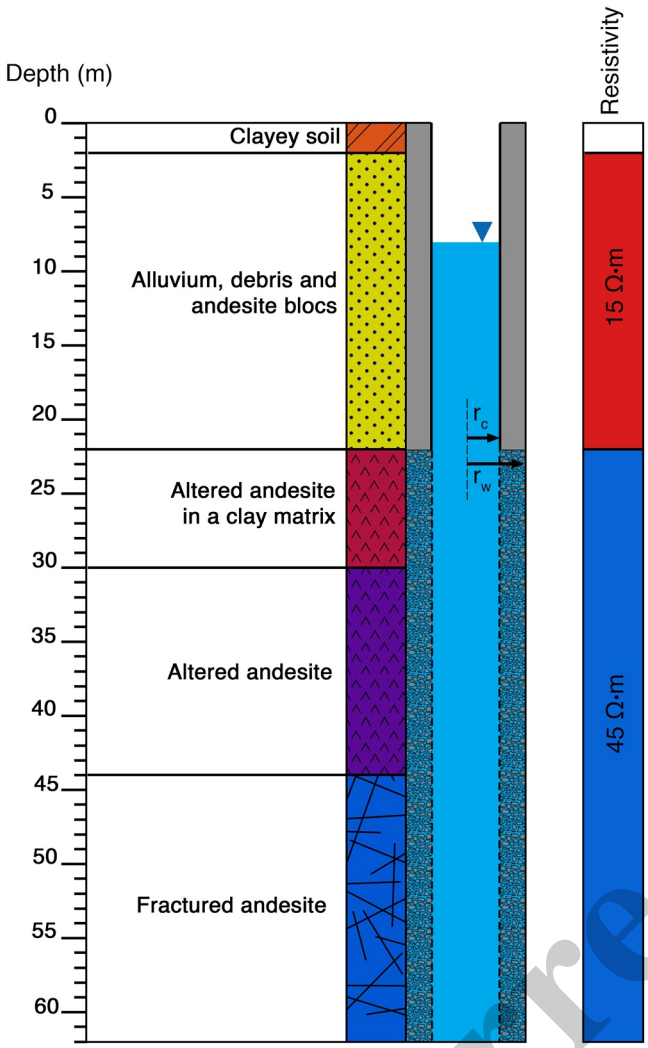

Figure 2. Geological borehole log. The aquifer is made of two layers: the fracture andesite and the altered andesite. The layer « altered andesite in a clay matrix" forms a cap rock. Thus, the aquifer layers (fractured andesite + altered andesite) are confined.

shaft encoder with integrated data logger, and SEBA Dipper-PT data logger, from 2014 to 2022, a ceramic pressure sensor, with integrated air pressure compensation tube.

Tidal signals could not be analyzed on some intervals between May 2010 and April 2013 due to sensor malfunction. Pumpings from late 2018 in a borehole situated 180 m upstream, with either high drawdown or on a daily rhythm, created spurious signal in the tidal frequency band. Thus, we focus the signal study during two timeseries: from February 2008 to April 2010 and from May 2013 to August 2018. Data which has been rejected is signaled in dark blue on Figure 3a. The barometric data as well as rainfall data have been purchased from the French meteorological agency nearest station, 5.3 km south east of Fond Lahaye (Figure 1c). Barometric data is measured hourly with a digital barometer PTB220 – VAISALA. Rainfall data is presented on a daily basis (Figure 3b) until early 2018, which covers the whole studied interval. Synthetic Earth tidal strain data have been generated with the function ertid of the SPOTL software (Agnew, 2012). Areal strain was converted to volumetric strain with an hypothesis of a Poisson ratio of 0.3 (Doan et al., 2008, eq 2.17).

2.3. Pumping Tests

Pumping tests were conducted in 2007, 2008 (Vittecoq & Brugeron, 2008), 2013 and 2022. The three firsts correspond to long terms pumping tests (72 hr for the two first and 42 days for the third one) conducted in a borehole 190m upstream in the Fond Lahaye valley (National number 1177ZZ0177). The studied borehole was used as a piezometer thus the interpretation yielded the storativities as well as hydraulic conductivities. The fourth pumping test was a short term one (4.5 hr), conducted in the studied borehole itself, with no piezometer. Data was analyzed with the MLU software (Carlson & Randall, 2012), which analytically solves drawdown in a multi-layered system. Results from pumping tests, used to validate a posteriori the model, are presented in Section 4.7.

3. Tidal Analysis

3.1. Tidal Analysis Method

The first step is to analyze the piezometric signal to compute barometric and earth tidal response functions. Practically response functions are (a) the amplitude ratio and (b) the phase lag between each source term (barometric and earth tide) and the response measured in the piezometric level.

Piezometric level in the borehole can be decomposed as a trend superposed to a tidal response:

$$h_w(t) = h_{w,trend}(t) + h_{w,tidal}(t)\,. \tag{1}$$

We are interested in the tidal signal which we obtained by filtering the signal with a Butterworth bandpass filter of order 4 with cutoff frequencies of 0.7 and 2.6 cpd (cycles per day). This signal can be written as the sum of cosine of known frequencies as predicted by tidal theory (Agnew, 2015):

Figure 1. (a) Localization of Martinique in the Caribbean plate. Caribbean plate boundary (dark line) and approximate North/South American plate boundary (white shading) from (Braszus et al., 2021) (b) Localization of the 128 felt earthquakes in Martinique reported by the OVSM-IPGP observatory during the period 2007–2019. Four strongest earthquakes: M7.4–2007/11/29 (hypocentral distance—hd: 165 km), M6.5–2014/02/18 (hd: 219 km), M6.6–2015/07/16 and M5.6–2017/02/03 (hd: 91 km). Digital elevation model from the General Bathymetric Chart of the Ocean (gebco.net), White arrow: vector of convergence (DeMets et al., 2000), main faults, ridges and subduction trench (Leclerc, 2014). (c) Localization of the Fond Lahaye Borehole, the ocean tide gauge (Fort-de-France harbor), the barometer (barometric pressure data) and the rain gauge station. Figure performed using ArcGis 10.5.1 (https://www.esri.com/).

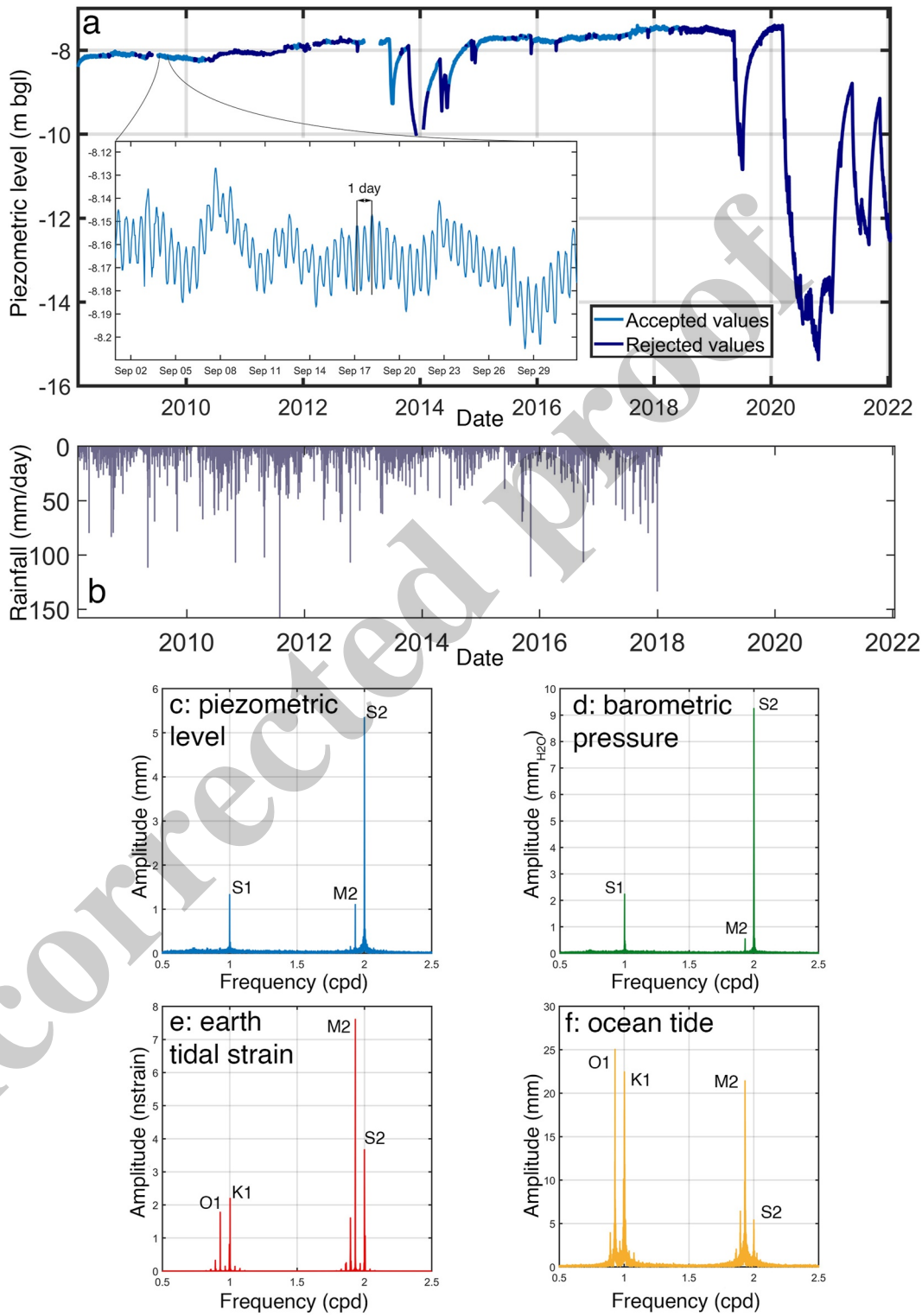

Figure 3. (a) Piezometric level (m below ground level) of the Fond Lahaye borehole time series (2008–2022), with a 1-month zoom on September 2009. Color indicates whether the data was used or not in the computation of the transfer functions. (b): Rain gauge data from Fort-de-France Desaix station (Figure 1c), in mm/day (c). (d, e, f): Frequency spectrums of piezometric level, barometric pressure, earth tidal strain and oceanic tide respectively. Each frequency is designated by its Darwin symbol (O1: 0.9295 cpd, S1: 10,000 cpd, K1: 1.0027 cpd, M2: 1.9322cpd, S2: 2.0000 cpd (Agnew, 2015), cpd: cycles per day).

$$h_{w,tidal}(t) = \sum_{k=1}^{n} A_k \cos(\omega_k t + \varphi_k)\,. \tag{2}$$

With ω_k, ϕ_k and A_k the angular frequency and corresponding phase and amplitude respectively. Or in complex notation:

$$h_{w,tidal}(t) = \sum_{k=1}^{n} \tilde{h}_{w,k} e^{i\omega_k t}, \tag{3}$$

with $\tilde{h}_{w,k}$ the complex amplitude. We recover each complex amplitude $\tilde{h}_{w,k}$ through a least square fit of sines and cosines at the known frequencies (Harmonic least square fit or HALS). Each HALS is performed on a 29 days window, the minimum width required to distinguish the two frequencies M2 and S2 (Agnew, 2015). The same treatment is applied to barometric pressure and earth tidal strain written as:

$$P_a(t) = \sum_{k=1}^{n} \tilde{P}_{a,k} e^{i\omega_k t}, \tag{4}$$

$$\varepsilon(t) = \sum_{k=1}^{n} \tilde{\varepsilon}_k e^{i\omega_k t}, \tag{5}$$

with $\tilde{P}_a$ and $\tilde{\varepsilon}$ the complex amplitudes. Within the framework of the linear theory of poroelasticity, we assume each frequency component of the piezometric signal is the result of the sum of effects from atmospheric pressure and earth tidal strain:

$$\forall k \in [\![1, n]\!], \tilde{h}_{w,k} = \frac{1}{\rho g}\left(Z_{baro,k} \cdot \tilde{P}_{a,k} + Z_{\varepsilon,k} \cdot \tilde{\varepsilon}_k\right) \tag{6}$$

In general, we are left for each frequency with one equation and two unknowns: the transfer functions $Z_{baro,k}\,[-]$ and $Z_{\varepsilon,k}[Pa]$ which are frequency dependent. To solve this problem in the case of tidal signals, we assume the transfer functions do not vary quickly with frequency, which was already done in Acworth et al. (2016) and more recently in Valois et al. (2022). This hypothesis will be discussed in Section 5.3. For two close frequencies ω_1 and ω_2, we can write:

$$\begin{aligned} \rho g \tilde{h}_{w,1} &= Z_{baro,12} \cdot \tilde{P}_{a,1} + Z_{\varepsilon,12} \cdot \tilde{\varepsilon}_1 \\ \rho g \tilde{h}_{w,2} &= Z_{baro,12} \cdot \tilde{P}_{a,2} + Z_{\varepsilon,12} \cdot \tilde{\varepsilon}_2 \end{aligned} \tag{7}$$

This linear system is solved as:

$$\begin{aligned} Z_{\varepsilon,12} &= \rho g \frac{\tilde{P}_{a,1} \cdot \tilde{h}_{w,2} - \tilde{P}_{a,2} \cdot \tilde{h}_{w,1}}{\tilde{P}_{a,1} \cdot \tilde{\varepsilon}_2 - \tilde{P}_{a,2} \cdot \tilde{\varepsilon}_1} \\ Z_{baro,12} &= \rho g \frac{\tilde{\varepsilon}_2 \cdot \tilde{h}_{w,1} - \tilde{\varepsilon}_1 \cdot \tilde{h}_{w,2}}{\tilde{P}_{a,1} \cdot \tilde{\varepsilon}_2 - \tilde{P}_{a,2} \cdot \tilde{\varepsilon}_1} \end{aligned} \tag{8}$$

This method enables to disentangle accurately the effects of barometric and earth tidal loading in the case of a pair of close frequencies. This is the case for the most studied semidiurnal tides M2 and S2 (Agnew, 2015) at 1.93 and 2 cpd (cycles per day) respectively, or the diurnal couple O1 S1 at 0.93 and 1 cpd. This method is useful to study both responses to atmospheric loading and earth tides. Studies addressing either atmospheric loading or earth tides are numerous (Acworth et al., 2016; He, 2016; Rojstaczer & Agnew, 1989; Rojstaczer & Riley, 1990; H. Zhang et al., 2019). Recently this method was implemented to combine both signals, namely by Rau et al. (2022) or Valois et al. (2022).

3.2. Tidal Analysis Results

The frequency spectrums of piezometric level, barometric pressure, earth tidal strain and oceanic level are represented respectively on Figures 3c, 3d, 3e and 3f. Given the two first spectrum similarities (Figures 3c and 3d), it appears that the piezometric level response is mostly driven by barometric pressure. Barometric pressure is also the only source that has a S1 frequency (1.0000 cpd) which is close but distinguished from the K1 frequency

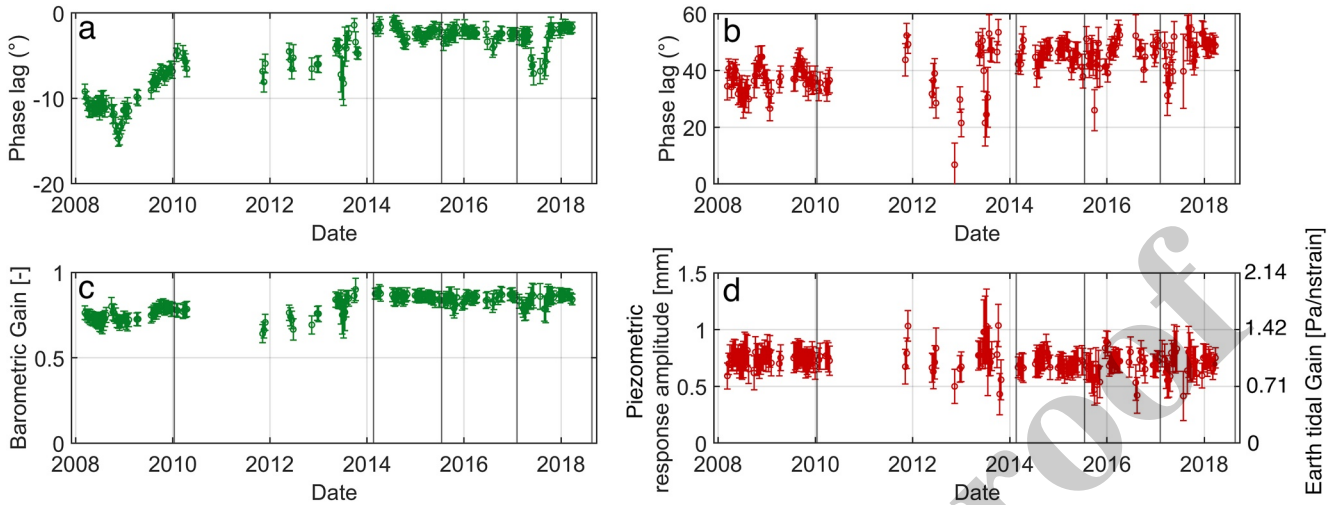

Figure 4. Evolution of the transfer functions over the last 10 years (a) Barometric and (b) Earth tide phase lags versus time. (c) Barometric gain and (d) Piezometric response to earth tide amplitude (in mm – left - and in Pa/nstrain - right) versus time. Dark vertical lines correspond to the main earthquakes in the region (discussed in Section 5.1).

(1.0027 cpd), presented by both oceanic and earth tides. Yet the increase in M2 amplitude relatively to S2 in these spectrum (Figures 3c and 3d) reveals another contribution either from earth tide or oceanic tide that cannot be neglected. If the additional contribution would come from oceanic tide (Figure 3f), a significant peak in O1 should have been observed in the piezometric level (Figure 3c), which is not the case. Thus, oceanic tide contribution is neglected before earth tide; this assumption will be discussed in Section 5.3. Finally, a complete tidal analysis as described in Section 3.1 was performed. Using M2 and S2 frequencies as ω_1 and ω_2, equation (8) yields the two transfer functions represented on Figure 4, on which each point corresponds to a 29 days window, and two adjacent points are 10 days apart. The barometric phase lag (Figure 4a) is defined as $-\arg\left(Z_{baro,M2/S2}\right)$ so that the phase lag is around 0° and not ± 180°.This barometric phase lag corresponds to $\arg\left(\frac{\rho g\tilde{h}_w^*}{-\tilde{P}_a}\right)$ where the superscript * refers to the piezometric level response to a single source, that is, barometric loading in this case, which is different from the measured piezometric level. We measure a negative phase lag for barometric pressure, starting from around −10° in 2008, increasing to −5° between 2008 and 2010, seemingly to stabilize around −3° from 2014, yet knowing some perturbations that will be discussed in Section 5.1. The amplitude response $|Z_{baro,M2/S2}|$, that is, the barometric gain, $|\frac{\rho g\tilde{h}_w^*}{-\tilde{P}_a}|$, shows the same global trend, increasing from 0.7 in 2008 to 0.9 in 2014 and then fluctuating around the value of 0.9, indicating that around 90% of the barometric signal is retrieved in the piezometric level.

The earth tide phase lag (Figure 4b) is defined as $\arg\left(Z_{\varepsilon,M2/S2}\right)$. This phase lag corresponds to $\arg\left(\frac{\rho g\tilde{h}_w^*}{\tilde{\varepsilon}}\right)$ where the superscript * refers to the piezometric level response to a single source, that is, the earth tide in this case, which is different from the measured piezometric level. The earth tide gain used in this article will be $G = |Z_{\varepsilon,M2/S2}| = |\frac{\rho g\tilde{h}_w^*}{\tilde{\varepsilon}}|$, except in Figures 6 and 15 where the gain is normalized to $G_n = |\frac{\rho g\tilde{h}_w^*}{BK_u\tilde{\varepsilon}}|$ to facilitate comparison with the literature. The earth tide amplitude response (Figure 4d) is expressed either in Pa/nstrain (unit of G), or in mm of piezometric head. In the latter case, the response is computed as $\frac{|\varepsilon_{M2}|}{\rho g}|Z_{\varepsilon,M2/S2}|$; it is proportional to $G = |Z_{\varepsilon,M2/S2}|\,[Pa/nstrain]$, because ρ, g and earth tidal strain amplitude $|\varepsilon_{M2}|$ are constant. The earth tidal signal, as expected given the amplitude spectrum (Figure 3d), is small and explains less than 1 mm of head oscillation in the borehole over a total oscillation of around 2 cm (Figure 3a), whereas approximately 1.9 cm is related to atmospheric loading. This relative faintness for earth tide explains why the phase lag signal (Figure 4b) is much noisier, even if a global increasing trend from a mean of 37° before 2013 and a mean of 45° between 2013 and 2018 can be noticed. There is no clear trend in the earth tide amplitude from 2008 to 2018.

The existing models that predict a positive phase lag for earth tide all require a source term due to vertical flow, either in the form of pressure diffusion to the water table or leakage to another layer, like in (Rojstaczer, 1988; Wang et al., 2018). They both hypothesize a constant head boundary condition on top, which is consistent in

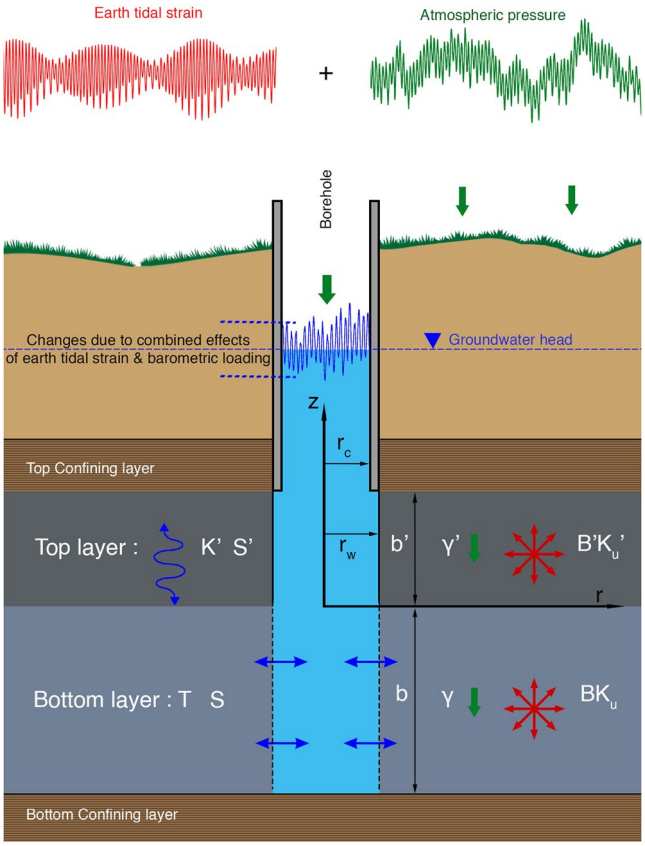

Figure 5. Conceptual model of a confined bi-layer aquifer. A bilayer aquifer is submitted to periodic sources of defined frequencies: earth tidal strain and barometric pressure. The water level in a well opened to this aquifer responds to the sources. The phase and amplitude of the response is a function of hydrodynamic (transmissivity T and storativity S of the bottom layer, vertical hydraulic conductivity K' and storativity S' of the top layer), poroelastic (Loading efficiency γ & γ', Skempton coefficients time undrained bulk moduli BK_u & $B'K'_u$) as well as geometrical parameters (layer width b & b', well and casing radii r_w & r_c). The radial axis r and the vertical z correspond to the reference frame used to describe the boundary conditions. Adapted from McMillan et al. (2019).

the presence of a water table aquifer. Yet, in these two cases the barometric phase lag observed in an open well should be the same as the earth tide phase lag—considering the minus sign on the definition of the barometric phase, that is, $\arg\left(\frac{\rho g h_w}{-P_a}\right)$. Because we observe a negative phase lag for barometric tide and a positive phase lag in the earth tide, we will derive in the next section a new model adapted to our geological observations (Figure 2). This model will also differ by the fact that it makes no further assumptions on layer parameters, like equal loading efficiencies between the two layers done in Rojstaczer (1988), or negligible storage in the top layer done in (Wang et al., 2018). The derivation of the response (Section 4) will thus be more general and the inversion of the model adaptable to other sites, even if it will obviously require adapted justified assumptions.

4. Tidal Response of a Confined Bi-Layer Aquifer

4.1. Conceptual Model of a Confined Bi-Layer Aquifer

We here derive the response of a well level $h_w\,(m)$ opened to a confined bi-layer aquifer to barometric loading $P_a\,(Pa)$ and earth tidal strain $\varepsilon\,(nstrain)$. The derivation is presented in the case of barometric loading, but the differences between the two sources, which lay in the boundary conditions, are presented, as well as the final solution. The aquifer is supposed infinite in the horizontal direction, homogeneous and isotropic. Following the adaptation of the Hantush and Jacob (1955)'s model to tidal strain by Wang et al. (2018), the well is opened to the "bottom layer" of the aquifer where flow is supposed horizontal, thus radial by symmetry. In Fond Lahaye, the bottom layer (Figure 5) corresponds to the fractured andesite (Figure 2). This layer will drain a second layer (leakage), referred to as the "top layer", which corresponds in Fond Lahaye to the altered andesite (Figure 2). As in Wang et al. (2018), flow is assumed vertical in this layer, but contrary to it, storativity of the top layer is non-zero, thus vertical flow is diffusive. As the aquifer is confined by the clay matrix (Figure 2), the boundary conditions will be no-flow at the top and bottom confining layers (Figure 5). The hydraulic head $h\,(m)$ in the bottom layer follows the diffusion equation:

$$T\nabla^2 h + q = S\left(\frac{\partial h}{\partial t} - \frac{\gamma}{\rho g}\frac{\partial P_a}{\partial t}\right) \tag{9}$$

where h is the hydraulic head in the bottom layer, S the hydrogeological storage coefficient $(-)$, T the transmissivity of the bottom layer $\left(m \cdot s^{-2}\right)$, γ the loading efficiency of the bottom layer $(-)$, and $q\,\left(m \cdot s^{-1}\right)$ is the vertical leakage from the top layer. The boundary conditions are:

$$h(r,t) = h_\infty(t)\ at\ r = \infty, \tag{10}$$

$$h(r,t) = h_w(t) + \frac{P_a}{\rho g} \quad at\ r = r_w, \tag{11}$$

$$2\pi r_w T \left.\frac{\partial h}{\partial r}\right|_{r=r_w} = \pi r_c^2 \frac{\partial h_w}{\partial t}, \tag{12}$$

where r_c is the well casing inner radius and r_w the radius of the screened portion of the well (Figure 5). Note that we here solve for the response to barometric loading, but the same can be applied to earth tidal strain by substituting in Equation (9) the source term $BK_u\frac{\partial \varepsilon}{\partial t}$ to $\gamma\frac{\partial P_a}{\partial t}$, where B is the Skempton coefficient and K_u the undrained bulk modulus of the bottom layer. Boundary conditions are kept the same except for Equation (11), which applies

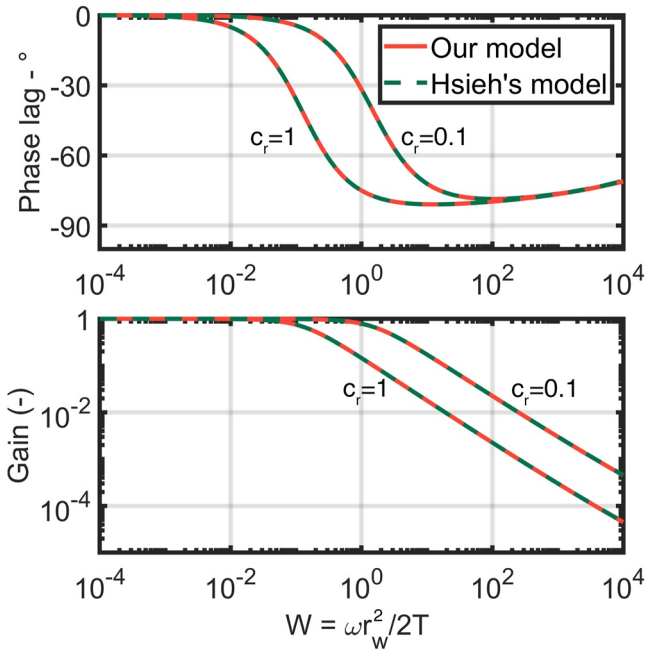

Figure 6. Red lines: Chart of the transfer function (eq 19 or eq 22) in terms of phase lag $\phi_n = arg\left(\frac{\rho g\tilde{h}_w}{(\gamma-1)\tilde{P}_a}\right)$ *or* $arg\left(\frac{\rho g\tilde{h}_w}{BK_u\tilde{\varepsilon}}\right)$ and adimensional (normalized) gain $G_n = |\frac{\rho g\tilde{h}_w}{(\gamma-1)\tilde{P}_a}|$ *or* $|\frac{\rho g\tilde{h}_w}{BK_u\tilde{\varepsilon}}|$, as a function of the borehole storage parameter W (In this abacus we assume no leakage effect, i.e., $Q = +\infty$). **Green lines:** Chart drown from Hsieh et al. (1987).

to an open well under barometric loading. For a closed well, a well equipped with a packer, or for earth tides, Equation (11) simplifies to

$$h(r_w, t) = h_w(t)$$

4.2. Top Layer Response: Computation of the Vertical Leakage q

Firstly, to get the expression of q we must solve for the excess pore pressure in the top layer, $p'(Pa)$. Since we assumed vertical flow, it follows a 1-D diffusion equation with a source term:

$$\frac{\partial^2 p'}{\partial z^2} = \frac{S'}{K'b'}\left(\frac{\partial p'}{\partial t} - \gamma'\frac{\partial P_a}{\partial t}\right) \tag{13}$$

where S' is the hydrogeological storage coefficient $(-)$, K' the vertical hydraulic conductivity of the top layer $\left(m \cdot s^{-1}\right)$, $b'(m)$ the width of the top layer and $\gamma'(-)$ the loading efficiency of the top layer (e.g., Wang, 2000). We are looking for periodic solutions at an angular frequency ω, thus physical quantity A will be expressed in the frequency domain by its complex amplitude labeled with a symbol $\tilde{A}$. The boundary conditions are, no flow on top:

$$\frac{\partial \tilde{p'}}{\partial z}_{|z=b'} = 0 \tag{14}$$

And pore pressure continuity at the layer interface:

$$\tilde{p'}(z=0) = \rho g\tilde{h} \tag{15}$$

with $\tilde{h}$ the complex amplitude of the hydraulic head in the bottom layer. The solution to this equation is (see Appendix A):

$$\tilde{p'}(z) = \left(\rho g\tilde{h} - \gamma'\tilde{P}_a\right)\left(\cosh\left(\sqrt{\frac{i\omega}{D'}}z\right) - \tanh\left(\sqrt{\frac{i\omega}{D'}}b'\right)\sinh\left(\sqrt{\frac{i\omega}{D'}}z\right)\right) + \gamma'\tilde{P}_a \tag{16}$$

with $D' = \frac{K'b'}{S'}$ the hydraulic diffusivity of the top layer $\left(m^2 \cdot s^{-1}\right)$, ρ water density $(kg \cdot m^{-3})$ and g gravity acceleration $(m \cdot s^{-2})$. We see in this intermediate result the dimensionless parameter $Q = \frac{b'^2\omega}{2D'}$ defined by Rojstaczer (1988). Thus, the source term $\tilde{q}$ in the bottom layer will be:

$$\tilde{q} = \frac{K'}{\rho g}\frac{\partial \tilde{p'}}{\partial z}_{|z=0} = -\frac{K'}{b'}\left(\tilde{h} - \frac{\gamma'}{\rho g}\tilde{P}_a\right)(1+i)\sqrt{Q}\cdot\tanh((1+i)\sqrt{Q}) \tag{17}$$

4.3. Whole Aquifer Response: Computation of the Head in the Well $\tilde{h}_w$

Now we may solve the hydraulic head in the bottom layer. Assuming radial symmetry, and injecting (17) in (9), $\tilde{h}$ follows:

$$T\left(\frac{\partial^2\tilde{h}}{\partial r^2} + \frac{1}{r}\frac{\partial\tilde{h}}{\partial r}\right) - \frac{K'}{b'}\left(\tilde{h} - \frac{\gamma'}{\rho g}\tilde{P}_a\right)(1+i)\sqrt{Q}\cdot\tanh((1+i)\sqrt{Q}) = i\omega S\left(\tilde{h} - \frac{\gamma}{\rho g}\tilde{P}_a\right) \tag{18}$$

From here the solving process is the same as in Wang et al. (2018), thus it is left in Appendix B. The general solution we obtain is:

$$\frac{\rho g\tilde{h}_w}{-\tilde{P}_a} = \left(\frac{(1-\gamma') + (1-\gamma)\cdot\frac{S}{S'}\frac{(1+i)\sqrt{Q}}{\tanh((1+i)\sqrt{Q})}}{1 + \frac{S}{S'}\frac{(1+i)\sqrt{Q}}{\tanh((1+i)\sqrt{Q})}}\right)\cdot\frac{1}{\xi} \tag{19}$$

Table 1
Phase Lag Sign, in the Absence of Borehole Storage, Depending on the Relative Values of Corresponding Poroelastic Parameters

Barometric tide		Earth tide	
$\gamma < \gamma'$	$\gamma > \gamma'$	$BK_u < (BK_u)'$	$BK_u > (BK_u)'$
+	−	−	+

where

$$\xi = 1 + i \cdot c_r \frac{W}{\beta r_w} \frac{K_0(\beta r_w)}{K_1(\beta r_w)} \tag{20}$$

$$\beta r_w = \sqrt{W}\left(\frac{(1+i)\tanh((1+i)\sqrt{Q})}{\sqrt{Q}} S' + 2iS \right)^{\frac{1}{2}} \tag{21}$$

where K_o and K_1 are the modified Bessel functions of the second kind, respectively of the zeroth and first order and $W = \frac{r_w^2 \omega}{2T}$. In the case of Earth tide response, the solution, detailed in the appendix, is:

$$\frac{\rho g \tilde{h}_w}{\tilde{\varepsilon}} = \left(\frac{B'K_u' + BK_u \cdot \frac{S}{S'} \frac{(1+i)\sqrt{Q}}{\tanh((1+i)\sqrt{Q})}}{1 + \frac{S}{S'} \frac{(1+i)\sqrt{Q}}{\tanh((1+i)\sqrt{Q})}} \right) \cdot \frac{1}{\xi} \tag{22}$$

To study both responses in parallel, it is useful to note that substituting the source $\tilde{P}_a$ by $\tilde{\varepsilon}$ can be achieved in the response by substituting the poroelastic parameters $(\gamma - 1)$ by BK_u and $(\gamma' - 1)$ by $B'K_u'$. That said, both responses are controlled by the same four adimensional parameters:

$$W = \frac{r_w^2 \omega}{2T}; \quad c_r = \left(\frac{r_c}{r_w} \right)^2; \quad Q = \frac{b'^2 \omega}{2D'} \text{ and } \frac{S}{S'}.$$

4.4. Physical Meaning of the Four Adimensional Parameters

Firstly, W and c_r were defined in Hsieh et al. (1987) in the case of earth tide and dictate the borehole storage effect, that is, a concurrent negative phase lag and attenuation. As shown on Figure 6, our model with $D' = 0$ is in perfect agreement with the model of a confined aquifer of Hsieh et al. (1987). It is important to note that in this case, the phase lag and gain for barometric pressure and earth tide are the same. A low W indicates a low borehole storage effect, which vanishes as soon as $W c_r < 10^{-2}$ (Figure 6 and Hsieh et al., 1987), while a high W indicates a strong borehole storage effect. c_r modulates this effect given the geometry of the borehole (Figure 6; Table 1) and equals in our case to $c_r = \left(\frac{r_c}{r_w} \right)^2 = 0.42$.

A second effect adds up to this first: the leakage effect, which is controlled by Q and $\frac{S}{S'}$. This effect is illustrated in the case of phase lag and gain for barometric pressure on Figures 7c and 7d, respectively and in the case of phase lag and gain for earth tide on Figures 7a and 7b, respectively. In Figure 7, we assume no borehole storage effect, that is, $W c_r < 10^{-2}$. The interpretation is less straightforward since now there are 3 distinct regimes (as identified in the case of barometric loading by Rojstaczer (1988)).

- A high frequency regime ($\sqrt{Q}\frac{S}{S'} \gg 1$, right of sub-figures 7) where the diffusion is negligible and the flow is controlled by the bottom layer. Phase lag tends to 0° in both earth tide (Figure 7a) and barometric loading (Figure 7c). According to Figure 7d), the barometric gain is equal to $(1 - \gamma)$ (bottom layer loading efficiency) and the earth tide gain is equal to BK_u. We assumed this regime when studying independently the borehole storage effect on Figure 6.
- A low frequency regime (on the left of sub-Figure 7, when $\sqrt{Q}\frac{S}{S'} \ll 1$), where vertical diffusion is strong enough so that the two layers are coupled: phase lag is 0° in both earth tide and barometric loading (Figures 7a and 7c) and the amplitude is controlled by the poroelastic coefficient of the layer with highest storage. More precisely it equals to the weighted mean $\frac{S'(1-\gamma') + S(1-\gamma)}{S' + S}$ for barometric gain and tends to $1 - \gamma'$ when $S \ll S'$ (Figure 7d) and equals to $\frac{S'B'K_u' + SBK_u}{S' + S}$ and tends $B'K_u'$ when $S \ll S'$ to for earth tide gain (Figure 7b).

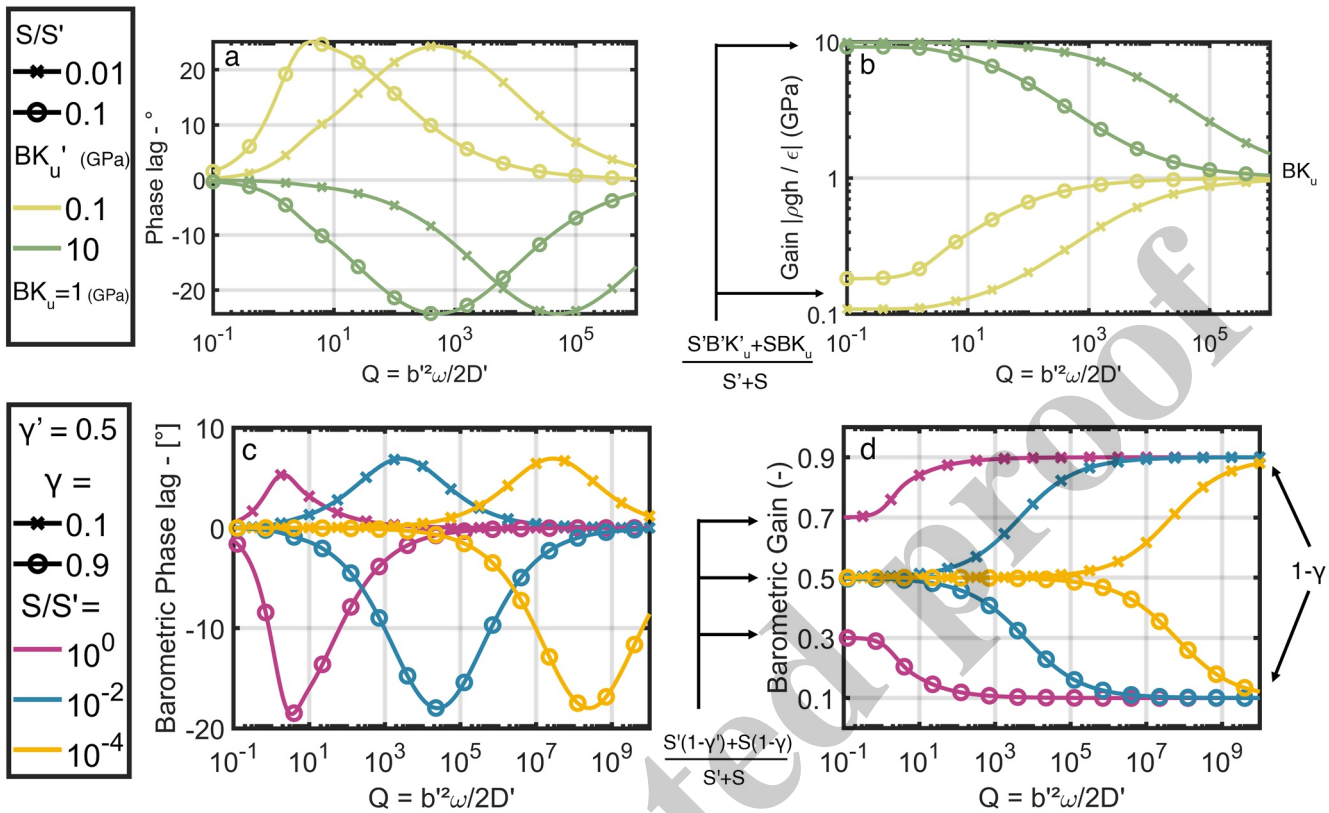

Figure 7. Chart of the transfer functions for earth tide (eq 22): (a) Phase lag $\phi = arg\left(\frac{\rho g \tilde{h}_w}{\tilde{\epsilon}}\right)$ and (b) gain $G = |\frac{\rho g \tilde{h}_w}{\tilde{\epsilon}}|$. For barometric pressure (Equation 19): (c) Phase lag $\phi = arg\left(\frac{\rho g \tilde{h}_w}{-\tilde{P}_a}\right)$ and (d) gain $G = |\frac{\rho g \tilde{h}_w}{-\tilde{P}_a}|$, as a function of the adimensional parameter Q (In this chart we assume no borehole storage, i.e., $Wr_c < 10^{-2}$).

- An intermediate frequency regime ($\sqrt{Q}\frac{S}{S'} \sim 1$) where phase shift occurs thanks to the exchange between the layers. The phase shift sign depends on the relative values of the poroelastic parameters (Table 1). The phase lag maximum or minimum values attainable are controlled by the contrast between these parameters, (higher contrast induces larger phase lag). In this regime, amplitude smoothly varies between the two previous extreme amplitudes.

4.5. Model Constraint

If the model encompasses many possible behaviors, we will show that looking at the phase shifts related to earth and barometric tides enables to constrain the model down to a few varying parameters that can be inverted.

Firstly, earth tide phase lag gives out a lot of information. Figure 8a shows the maximum attainable earth tide phase lag for all value of Q, BK_u, $B'K'_u$ as a function of W and S/S'. The mean earth tide phase lag in the Fond Lahaye borehole varies between 37° (before 01/2013) and 45° (after 01/2013) (red dotted lines on Figures 8a and 8b). Thus, from Figure 8a, we can infer that the borehole storage effect must be negligible at least starting from 2013 (since borehole storage only decreases the phase lag), and that $W = \frac{r_w^2 \omega}{2T} \leq 10^{-2}$. The remaining question, is whether borehole storage (change in W) or vertical diffusion (change in Q) is responsible for the change in phase lag between these two intervals. A change in parameter W implies that phase lag increases simultaneously and with the same amount for barometric pressure and earth tidal signals (Figure 6). Yet, the clear increasing trend observed in barometric phase lag in 2009/2010 (Figure 4a) is not seen on earth tide (Figure 4b), which increase occurred between 2011 and 2013. Because the changes in phase lag are not simultaneous, we

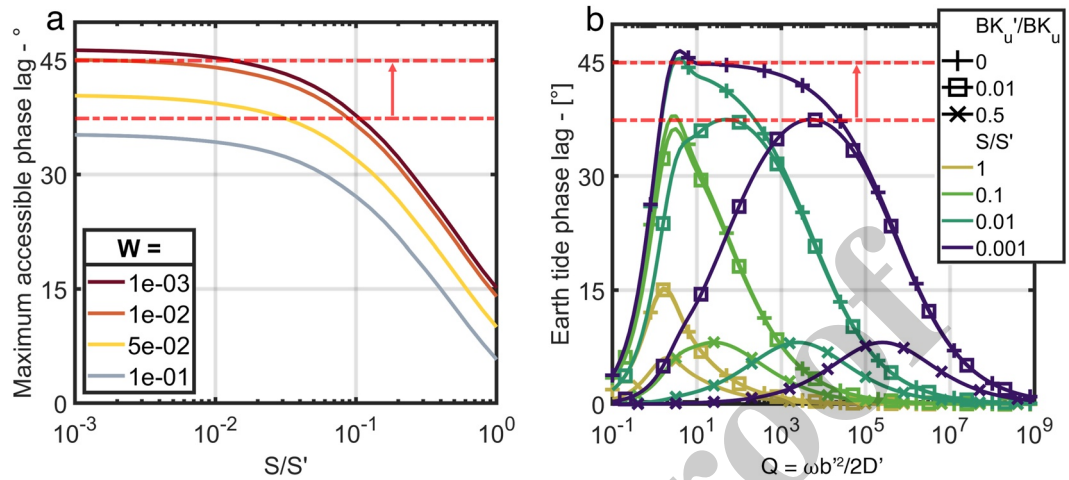

Figure 8. (a) Maximum attainable earth tide phase lag $\phi = arg\left(\frac{\rho g \tilde{h}_w}{\tilde{\varepsilon}}\right)$ for all values of Q, BK_u and $B'K'_u$, depending on W and $\frac{S}{S'}$. Maximum values are obtained setting $B'K'_u = 0$ (b) Chart of earth tide phase lag ϕ predicted by the model for different values of S/S' and $\frac{B'K'_u}{BK_u}$, with neglectable borehole storage effect ($W \ll 1$). The maximum of the curve with $B'K'_u = 0$ (label '+') on (b) corresponds to a dot for a given S/S' on (a) for $W = 10^{-3}$. a & b, red dotted lines: mean observed earth tide phase lag before and after 01/2013.

conclude that borehole storage (adimensional parameter W) is negligible for the whole studied period and set $W = \frac{r_w^2 \omega}{2T} \leq 10^{-2}$, which translates in our response functions Equations (19 & 22), in:

$$\xi = 1. \tag{H1}$$

Figure 8b, shows the evolution of earth tide for different values of Q, $B'K'_u/BK_u$ and S/S' with the hypothesis $W \leq 10^{-2}$. Our data range between 37° (before 01/2013) and 45° (after 01/2013) (red dotted lines). The positive sign of the phase lag tells us that $BK_u > B'K'_u$ (Table 1). In addition, the range of the observed phase lag induced a constrain on the ratio $B'K'_u/BK_u$ (Figure 8b) and the phase lags only be predicted if:

$$\frac{B'K'_u}{BK_u} < 10^{-2}. \tag{H2}$$

From Gassmann's equation (Gassman, 1951), we know that

$$BK_u = \frac{\alpha}{\frac{\phi}{K_f} + \frac{\alpha - \phi}{K_s}}, \tag{H3}$$

where α is the Biot coefficient, ϕ is the porosity, K_f the bulk modulus of the fluid and K_s the bulk modulus of the solid grain. The hypothesis ($H2$) implies that the top layer is more porous that the bottom layer and that grain bulks modulus of the top layer is lower than the one of the bottom layer. This is consistent with the geological observations (Figure 2) as the bottom layer is a fractured andesite (thus low porosity) and the top layer is made of altered andesite (higher porosity and lower grain bulk modulus).

Furthermore, when looking at Figure 8b, we can observe that our data are consistent with $\frac{S}{S'} \leq 0.01$, since only dark green and blue curves cross the range of observed data. Assuming constant storativities is common practice when dealing with variable hydrodynamic parameters, because phase responses are less sensitive to them (Hsieh et al., 1987; Rojstaczer, 1988; Wang et al., 2018). Thus, we chose to that the ratio $\frac{S}{S'}$ is constant (Hypothesis H3).

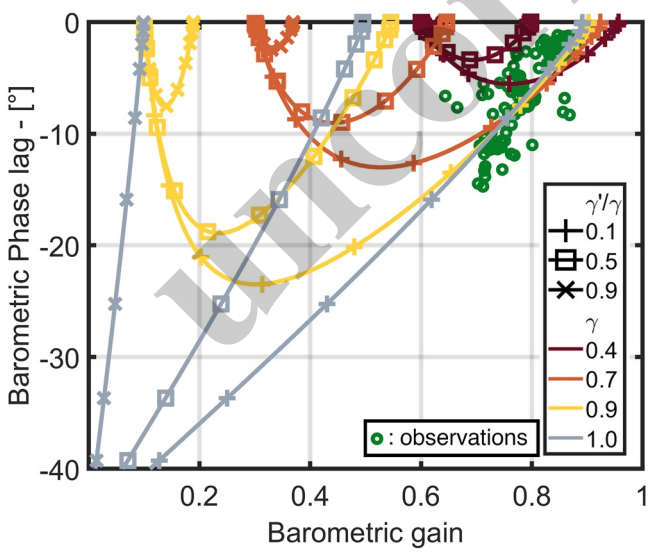

Figure 9. Colored lines: Phase/Amplitude diagram of the theoretical barometric response (*eq* 19), with $\xi = 1$ ($H1$), and varying $\sqrt{Q}\frac{S}{S'}$.The value of γ and the ratio γ'/γ is specified for each line. Green dots: observed barometric response points in the Phase/Amplitude space.

Besides, barometric response function also yields information. It is represented in a Phase/Gain diagram on Figure 9 for different value of γ (each color means a fixed value of γ) and γ'/γ. We already know that $\gamma' < \gamma$ given the negative phase lag (table 1), thus we explore the possible range of these poroelastic parameters. Our data appears in green in Figure 9. It appears that in the vicinity of data points, the model is quite insensitive to γ (the lines with different colors are close together), but far more sensitive to γ' (the lines with differing markers are spaced), which makes of γ a good candidate to be assumed constant. We observe on Figure 9 that to explain the entirety of phase lag variation, we need to set $\gamma \geq 0.9$. This is consistent with the geology of the bottom layer: compliant fractures in rigid andesite explain why all of the exerted pressure has an effect on pore pressure (Brajanovski et al., 2005; Gallagher et al., 2022). For the sake of simplicity, we set

$$\gamma \sim 1. \tag{H4}$$

If we do observe that the model is sensitive to the ratio γ'/γ, the ratio should be in the range 0.05–0.2 to explain our data. The last 3 hypotheses (H2, H3, H4) seem unrelated. Yet poroelasticity theory (Wang, 2000) tells us that $\gamma = B\frac{1+\nu_u}{3(1-\nu_u)}$, where ν_u is the undrained Poisson ration, and $S_s = \frac{\alpha}{K_v\gamma}$, where S_s is the uniaxial specific storage, α is Biot's coefficient and K_v the uniaxial drained bulk modulus. Thus, it is expected that:

$$\frac{B'}{B} \propto \frac{\gamma'}{\gamma} \propto \frac{S}{S'}, \tag{23}$$

which is consistent with our case where $\gamma' \ll \gamma$, $B'K'_u \ll BK_u$ and $S \ll S'$. In addition, the hypotheses are consistent with the geological observation: a bottom layer made of fractured andesite (small porosity, but very compressible) and a top layer made of altered andesite (higher porosity but less compressible).

4.6. Model Inversion

Thanks to the three assumptions ($H1-4$), Equation (19) reduces to:

$$\frac{\rho g \tilde{h}_w}{\tilde{P}_a} = \frac{\gamma' - 1}{1 + \frac{S}{S'}\frac{(1+i)\sqrt{Q}}{\tanh((1+i)\sqrt{Q})}} \tag{24}$$

This simplified model is able to cover the range −45 to 0° in terms of phase lag. We are left with three parameters: γ', Q, S/S'. We assume S/S' constant and we fix it at 10^{-2} ($H3$). Note that a change in the ratio S/S' will not the change fundamentally the results, especially the relative change of the hydrodynamic properties with time. Since we have two independent observations (Amplitude and phase lag) we can perform a numerical inversion of these last two parameters (Note that if $\sqrt{Q} > 10$, the inversion can be analytical – see appendix C). It yields the results presented on Figure 10.

Following the same process, and the three assumptions ($H1-3$), Equation (22) reduces to:

$$\frac{\rho g \tilde{h}_w}{\tilde{\varepsilon}} = \frac{BK_u \cdot \left(\frac{S}{S'}(1+i)\sqrt{Q} + \frac{B'K'_u}{BK_u}\right)}{1 + \frac{S}{S'}\frac{(1+i)\sqrt{Q}}{\tanh((1+i)\sqrt{Q})}} \tag{25}$$

Which covers the range 0 to +45° in terms of phase lag. Since $\frac{B'K'_u}{BK_u} \ll \frac{S}{S'}\sqrt{Q}$, we are left with two parameters: BK_u and Q. Again, a numerical inversion was performed, yielding the results presented in Figure 11.

Figure 10a shows the evolution of the diffusivity D'-deduced from the adimensional parameter Q-in the top layer infer from the barometric loading analysis (Equation 24). From 2008 to 2018, the diffusivity increases of more than one order of magnitude. In 2008, the diffusivity is found to be $2.5\,10^{-5}\,m^2/s$; it increases to a value of $10^{-4}\,m^2/s$ between 2010 and 2013, and increases again to a value of $5 \cdot 10^{-4} m^2/s$ between 2015 and 2018. In addition to the long-term evolution, several temporary changes: several increases or decreases of D' that can

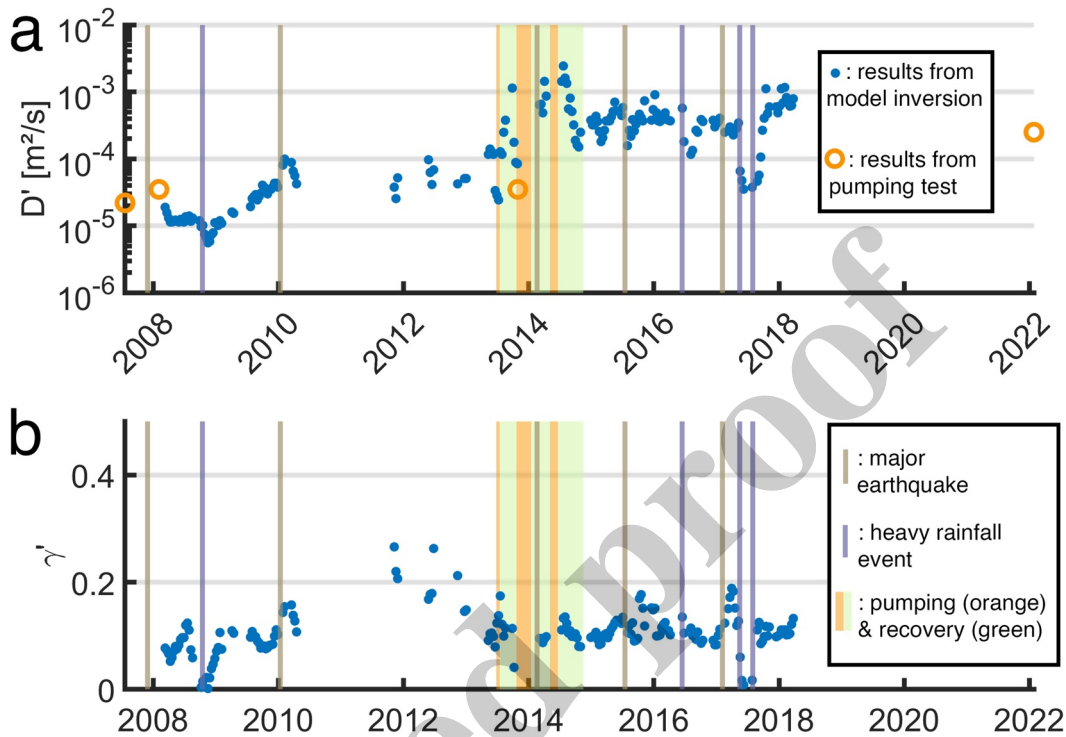

Figure 10. Evolution of (a) top layer vertical Diffusivity D' and (b) top layer loading efficiency γ' inverted from the barometric transfer function. The orange circles correspond to the results of pumping tests presented in (4.7). Vertical brown lines correspond to earthquakes, vertical blue lines correspond to heavy rainfall events and the orange/green rectangles to the pumpings for drinking water operation of the aquifer. Uncertainty on these parameters, which mainly comes from measurement uncertainty, are plotted in Figure S4 in Supporting Information S1.

be observed are transients. Such transient change of properties can also be observed on the loading efficiency (Figure 10b).

The evolution of the diffusivity can also be obtained independently from the earth tide analysis (Equation 25). Here we repeat that the piezometric oscillation amplitude are controlled by approximately 90% of the barometric loading and 10% of the earth tide loading. Even if the results (Figure 11a) are noisy and yield more uncertainty, the general tendency of the diffusivity D' is consistent with the previous one, with an average around $5 \cdot 10^{-5}\, m^2/s$ in 2008–2010 and $5 \cdot 10^{-4} m^2/s$ between 2013 and 2018. Yet it is far less interesting to study because it does not enable to identify transient behavior, and thus identify causes behind the observed evolutions. Finally, the evolution of BK_u is given in Figure 10b, with a mean value of 8 GPa, which seems to be a reasonable value (Bailly et al., 2019; Larochelle et al., 2022; Wang et al., 2018).

4.7. Validation With Pumping Tests

The key point is: can we be confident with the evolution of the diffusivity found by the tidal analysis (Figure 10a)? It turns out, that four pumping tests were done in this aquifer (Table 2). The characteristics and results of each pumping test are listed in Table 2. They were obtained with the MLU software which can reproduce the same geometry as described in Figure 5, with an analytical model similar to ours but adapted to pumping tests (Maas, 1987). MLU parameter optimizer was used to obtain the parameters (hydraulic conductivity and storage) yielding the best fit to the measured data. Measured data and fitted curves are presented in Figure S1 in Supporting Information S1, along with additional detail on MLU parameters. We will use these results to validate the model.

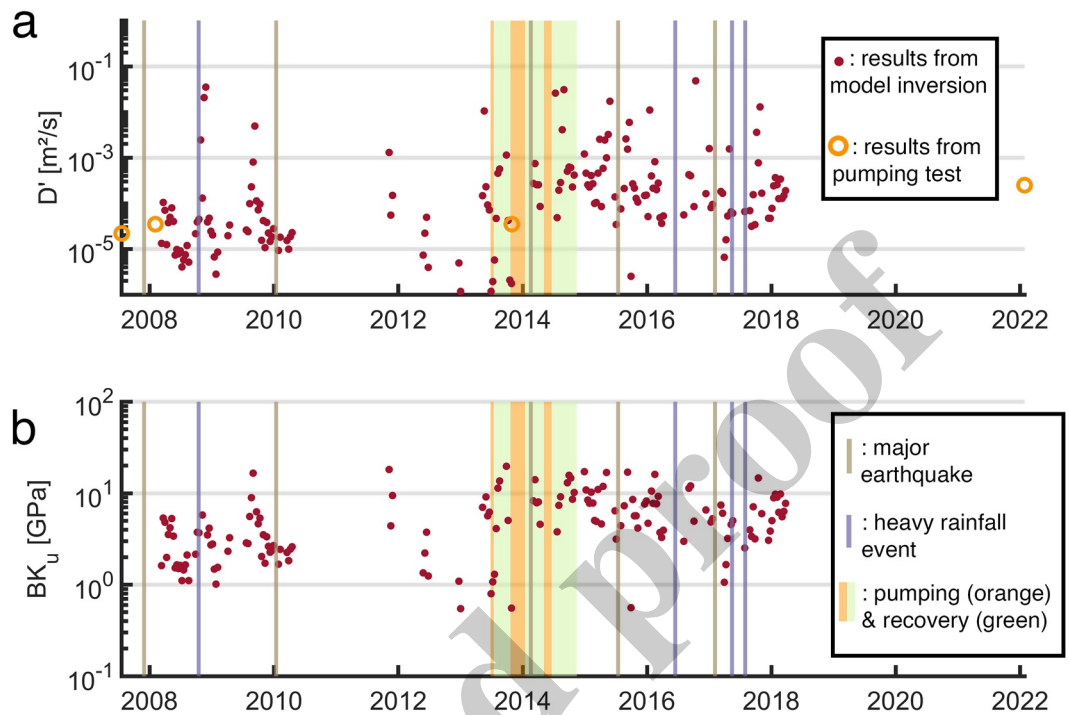

Figure 11. Evolution of (a) top layer vertical Diffusivity D' inverted from earth tide transfer function (b) $BK_u\,(GPa)$ with B the bottom layer Skempton coefficient and K_u the undrained bulk modulus. The orange circles correspond to the results of pumping tests presented in (4.7). Vertical brown lines correspond to earthquakes, vertical blue lines correspond to heavy rainfall events and the orange/green rectangles to the pumpings for drinking water operation of the aquifer.

First, the lowest measured transmissivity of the bottom layer obtained by pumping tests is $2.4 \cdot 10^{-4}\,m/\mathrm{s}$ (Table 2) yields $Wr_c \sim 10^{-5}$. This first observation validates the hypothesis ($H1$): the borehole storage effect is negligible because bottom layer transmissivity is high enough.

The second observation is that despite being less sensitive to S/S' than to transmissivity, all fitted curves of the pumping test analysis by the MLU software were compatible with a constant storativities (Hypothesis H3), and the pumping test analysis leads to $\frac{S}{S'} = 0.01$.

Finally, the results of the model in terms of top layer diffusivity are validated by these pumping tests, as seen on Figures 10a (and 11a). Both absolute values (from $D' = 10^{-5}$ to $10^{-4} m^2/\mathrm{s}$) and increasing trend are reproduced, and this despite the large discrepancy between the different conditions in which the pumping tests were conducted, as their duration, flow rate and pumping well (with or without observation well) changed between pumpings.

Table 2
Pumping Tests Characteristics and Results in Terms of Hydrodynamic Parameters

Year	Distance to pumping well	Duration	Flow rate (m^3/h)	Aquifer transmissivity $T\,(m^2/s)$	Top layer diffusivity $D'(m^2/s)$	Storativity ratio $S/S'(-)$
2007	180 m	72 hr	17.2	$5.7 \cdot 10^{-4}$	$2.2 \cdot 10^{-5}$	0.01
2008	180 m	72 hr	25.0	$5.23 \cdot 10^{-4}$	$3.5 \cdot 10^{-5}$	0.01
2013	180 m	42 days	30.0	$3.4 \cdot 10^{-4}$	$3.5 \cdot 10^{-5}$	0.01
2022	0 m	4.56 hr	3.5	$2.4 \cdot 10^{-4}$	$2.5 \cdot 10^{-4}$	–

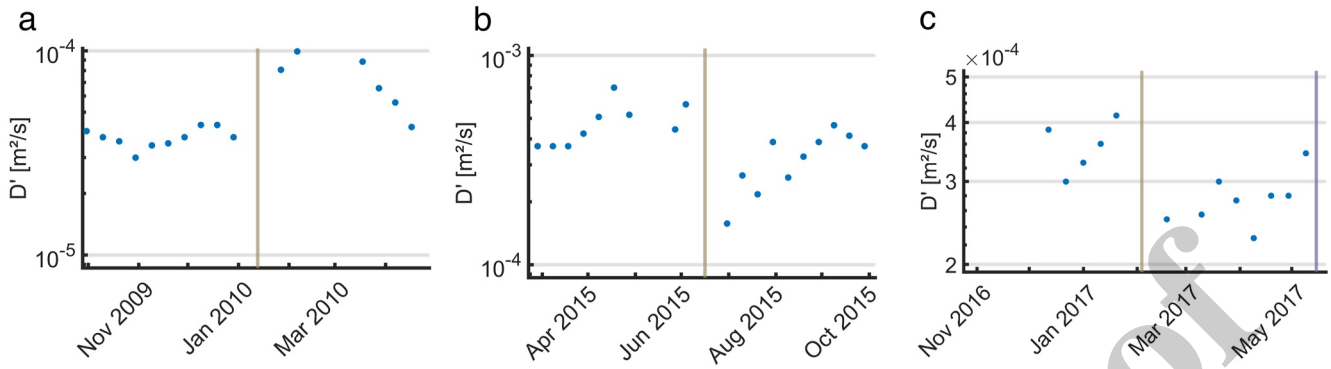

Figure 12. Zoom of Figure 10 on the different earthquakes effect on diffusivity: (a) 2010, (b) 2015, and (c) 2017.

5. Discussion

5.1. Evolution of the Hydrodynamic Properties Over Time

5.1.1. Impact of Earthquakes

Literature has identified earthquakes as a major cause for changes in properties of aquifers (Rojstaczer et al., 1995; C.-Y. Wang et al., 2004; Elkhoury et al., 2006; Manga et al., 2012; Vittecoq et al., 2020). In our case, it is possible to link four earthquakes to change in diffusivity thanks to tidal analysis and an additional one thanks to pumping tests. The two first are linked to transient increase: the 2007 for which pumping tests indicated an increase in top layer diffusivity from $2.2 \cdot 10^{-5} m^2/s$ to $3.5 \cdot 10^{-5} m^2/s$ (Figure 10, Table 2), and the 2010 one, for which diffusivity directly increased from $4 \cdot 10^{-5} m^2/s$ to $8 \cdot 10^{-5} m^2/s$, but came back to the initial value in 3 months (Figure 12a). We attribute these transient effects to unclogging of fractures, a phenomenon already reported both at the lab and field scale in numerous studies (Barbosa et al., 2019; Boeut et al., 2020; Candela, 2014; Elkhoury et al., 2011; Vittecoq et al., 2020; H. Wang et al., 2020). Unclogging of fractures have been shown to be most plausible phenomenon at stake in the intermediate field, where static strain change is too low to have significant impact and dynamic strains are too low to cause fracturation. Unclogging is able to explain the large variations in permeability observed, especially in fractured aquifer. The 2014 earthquake has also induced an increase in diffusivity. However, this earthquake occurred during a long-term pumping test, thus we cannot conclude if increase of diffusivity between 2013 and 2015 is related to the earthquake or to the pumping test. It is, however, interesting to note that this earthquake has induced a clear permanent increase of permeability in another aquifer of the island (Vittecoq et al., 2020).

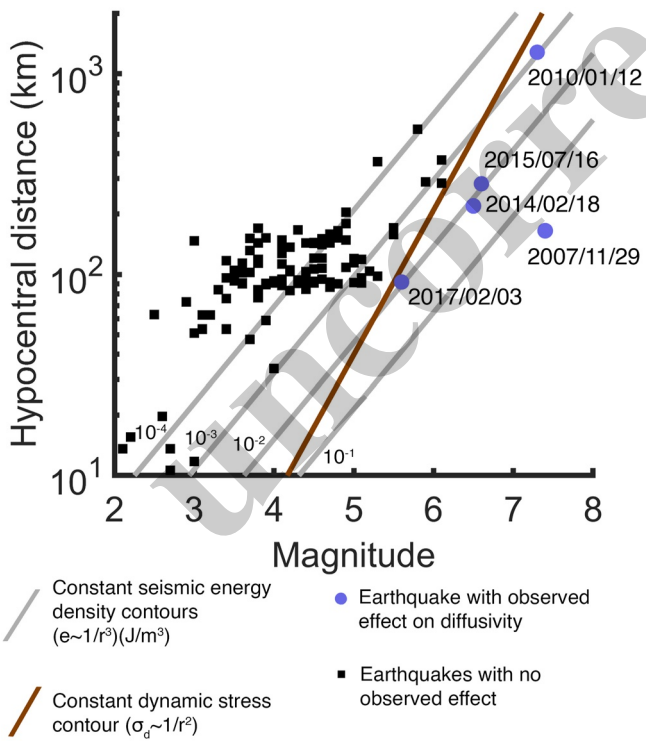

Figure 13. Magnitude/distance plot of the earthquakes felt in Martinique between 2007 and 2018. Gray oblique lines correspond to constant seismic energy density contours (J/m^3) (Wang & Manga, 2010) and dark red one to a constant dynamic stress contour.

The next two identified earthquakes induced transient decrease in the top layer diffusivity. In 2015 and 2017, diffusivity decreased from $5 \cdot 10^{-4} m^2/s$ and $3.5 \cdot 10^{-4} m^2/s$ before the earthquake to $2 \cdot 10^{-4} m^2/s$ after (Figures 12b and 12c). Permeability decrease were already reported, namely in Shi et al. (2019) or Vittecoq et al. (2020) which is attributed to clogging effect, this decrease in permeability is transient, and after 2–3 months, the initial value is recovered. This characteristic time of a few months can also be observed in the case of extreme rainfall events (Section 5.1.b), advocating for a similar process in both case, particle mobilization. Given we only observed three coseismic changes, it is difficult to be conclusive on a possible cause explaining why permeability would increase or decrease after an earthquake. Previous hypotheses include the azimuth and the focal mechanism of the earthquake, which is certainly relevant concerning near field effects, linked to static stresses, but less clearly in the case of dynamic strains effects although it is probably relevant in fractured aquifer where preferential

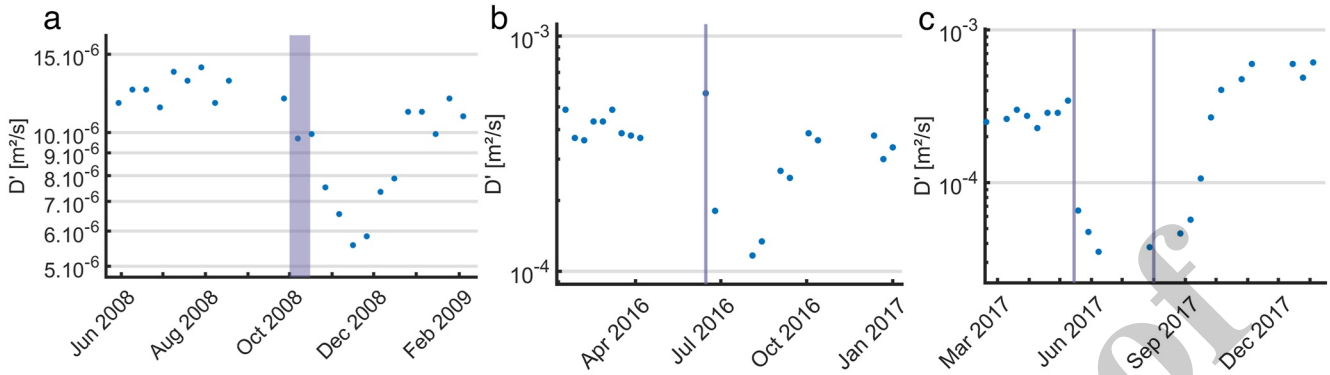

Figure 14. Zoom of Figure 10 on the different rainfall events effect on diffusivity: (a) 2008, (b) 2016 and (c) 2017.

fracture directions stand out (Shi et al., 2019; Xiang et al., 2019; Yan et al., 2014). If the underlying mechanism cannot be demonstrated here, an interesting information can be inferred from the magnitude/distance plot of the earthquakes that have an impact on the diffusivity (Figure 13). Roeloffs (1998), proposed a criterion for persistent water level drops or rise: $M \geq 1.88\log(r) + 1.55$, with M the magnitude and r the well-hypocenter distance in kilometers. This empirical criterion was generalized by Wang and Manga (2010), based on seismic energy density, and yields $M \geq 0.7\log\left(r^3\right) + E$, where E depends on the threshold of seismic energy density. These criterion were designed to explain water level changes in wells, which are generally different from permeability enhancement, as recognized in (Elkhoury et al., 2006; Wang & Manga, 2010). Here, such a criterion cannot explain why diffusivity evolved after the 2010 earthquake while it did not after many others of similar energy (Figure 13). We thus suspect that transient changes are better explained with a criteria on dynamic stress, which decreases as the square of the distance (Aki & Richards, 2002). We graphically set our threshold to be $M \geq 0.7\log\left(r^2\right) + 2.7$ (Figure 13), by drawing the line of corresponding slope that was directly above all earthquakes impacting permeability. On this figure, several earthquakes that were expected to have an impact could not be studied, either because they were outside of the exploitable signal, or like in 2014, concurrent with pumpings in the aquifer which have a strong impact on diffusivity. Trying to go further, we tried to relate the peak ground velocities (PGVs) to the amplitude of change in the permeability. Using measured peak ground velocities (PGVs) as a proxy to dynamic strain intensity, Elkhoury et al. (2006) observed a correlation between them. Yet to the best of our knowledge, no similar observations was made since then, as shown on Figure S3 in Supporting Information S1. This absence of correlation of the data might be explained as the PGV and change in the dynamic stress or strain is not straightforward.

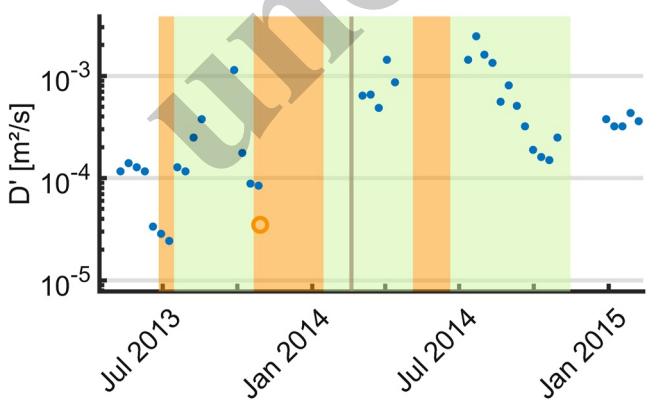

Figure 15. Zoom of Figure 10 on the consecutive pumpings in the aquifer in 2013/2014. Orange rectangles refer to pumpings and green periods to recovery. The brown vertical lines represent the 2014 earthquake.

5.1.2. Extreme Rainfall Events

A second phenomenon has been identified in a previous study in Martinique: strong rainfall events (Vittecoq et al., 2020). Three similar transient evolutions in the signal have been identified, in October 2008 July 2016 and May–August 2017. For these three events we observe a significant decrease in the diffusivity, which decreased by a factor 2 to six over a month, and a recovery over the same period (Figure 14). October 2008 was reported to be the third rainiest October month since the start of rainfall measurements in 1936. A total of 871 mm were recorded at the nearest station (Météo France, 2008), with several days over 100 mm. July 2016 was also exceptionally rainy with almost 500 mm reported, concentrated on a few days, while the consecutive months of May–August 2017 have known several events, from heavy rainfall to tropical storms, as already reported in (Vittecoq et al., 2020). Several mechanisms could explain the change in diffusivity. The first one is the fluidization of many solid particles like colloids. Theory predicts that adding particles in a fluid increases its viscosity. In the case of rigid spherical particles with no interaction,

Table 3
Vertical Diffusion Length in the Top Layer, for the Tidal Model and the Different Pumpings

	Tidal model (2008–2018)	2007 pumping	2008 pumping	2013 pumping	2022 pumping
δ (m)	1.9–9.9	4.8	5.8	32.0 (whole layer)	3.0

Note. The range depends mostly on the pumping duration and calculated vertical diffusivity.

in an incompressible fluid, the predicted change in viscosity is linked to volume fraction of particles such that:

$$\frac{\mu}{\mu_0} = \frac{1}{1 - \frac{5}{2}\phi}$$

where μ is the dynamic viscosity of water with a volume fraction ϕ of particles, and μ_0 the dynamic viscosity of water in the absence of particle (Kachanov & Abedian, 2015). This formula is in accordance with experimental data up to a volume fraction of 30% when the non-interaction hypotheses fades. It could explain an increase up to a factor 4 in the viscosity, thus a decrease in hydraulic conductivity and diffusivity by the same factor. This effect fades once the colloids are evacuated, at the same rate of their appearance. A second explanation involves the loading of the aquifer by temporary accumulation of rainfall water in the alluvium (Figure 2). Such an additional load would increase the effective pressure in the aquifer, closing pathways for water to flow. Both explanations would need further investigations to be tested, yet may contribute to the effect simultaneously. In both cases, the observed delay of around 1 month for onset and decay of the decrease could be explained by pressure diffusion and accumulation/drainage characteristic time.

5.1.3. Effect of Pumping in the Aquifer

We suspect a last phenomenon has had an impact on top layer diffusivity: long term pumping. It is difficult to analyze the effect of pumpings with tidal analysis during the pumping because if the piezometric level decreases to quickly, the tidal signal is lost. Yet we recovered many data points, especially during recovery periods, where we manually checked the quality of the signal because quickly varying piezometric signals can affect tidal analysis. With all due precautions, the impact of pumpings on diffusivity, which varied by a factor 40 over the 2013 pumping and a factor 15 over the 2014, cannot be regarded as a random scatter, yet its effects are not evident to analyze. Pumpings have a strong impact on the fluid velocity in the aquifer and on pore pressure. It seems that diffusivity decreases during a pumping (see Figure 15 on July 2013), where the decline of D' starts slightly before the pumping because of the 29 days' time window. We consider two possible mechanism have a transient effect during the pumping process: on the one hand particle mobilization in the fluid increases viscosity, that is, decreases hydraulic conductivity. On the other hand, the increase in effective pressure $\sigma^* = \sigma - p$ (here linked to the decrease in pore pressure) closes pathways for water, that is, reduces fracture aperture and permeability. The effect of recovery is more ambiguous, since during the first one diffusivity increased to recover its initial value. The second recovery cannot be analyzed because of a possible impact of the earthquake, and during the third one, diffusivity decreased. Further investigation would be needed to clearly conclude on the short-term impacts of pumpings on diffusivity. About the long term impact, it seems that here the diffusivity increased overall, which is understandable when considering that pumping can lead to unclogging, yet we cannot conclude as the 2014 earthquake was simultaneous and was shown to have had impacts on the hydraulic conductivity in another aquifer of the island (Vittecoq et al., 2020).

5.2. Diffusivity Inferred From Pumping Tests and From Tidal Analysis

Sensitivity to parameters is different between a pumping test, which is only sensitive to flow phenomena, and a tidal model, sensitive to poro-mechanical effects as well as flow ones. A pumping tests consists of a local perturbation, which is mostly sensitive to transmissivity and vertical permeability in our model, on a horizontal extent L depending on the pumping duration t_p and bottom layer diffusivity D: $L \sim \sqrt{Dt_p}$ (Méité et al., 2022), and on a vertical dimension $\delta_p \sim \sqrt{D't_p}$, with D' the vertical diffusivity in the top layer. Considering the tidal model, its sensitivity to parameters depend on the flow regime: in the absence of borehole storage effect, the head in the aquifer is homogeneous and the response does not depend on transmissivity. The relevant space dimension in our case is the width of the diffusive process in the top layer $\delta_t \sim \sqrt{\frac{2\pi D'}{\omega}}$. The different vertical diffusion lengths δ are summarized in table 3. Firstly, it appears that δ_t has evolved significantly during the decade 2008–2018 because of the increase of vertical diffusivity. And since the width of the top layer is 14m, it corresponds effectively to new regions of the layer being reached. Secondly, we can remark that the variety of the width investigated and pumping durations, the results are consistent, which consolidates the homogeneity assumption in our model.

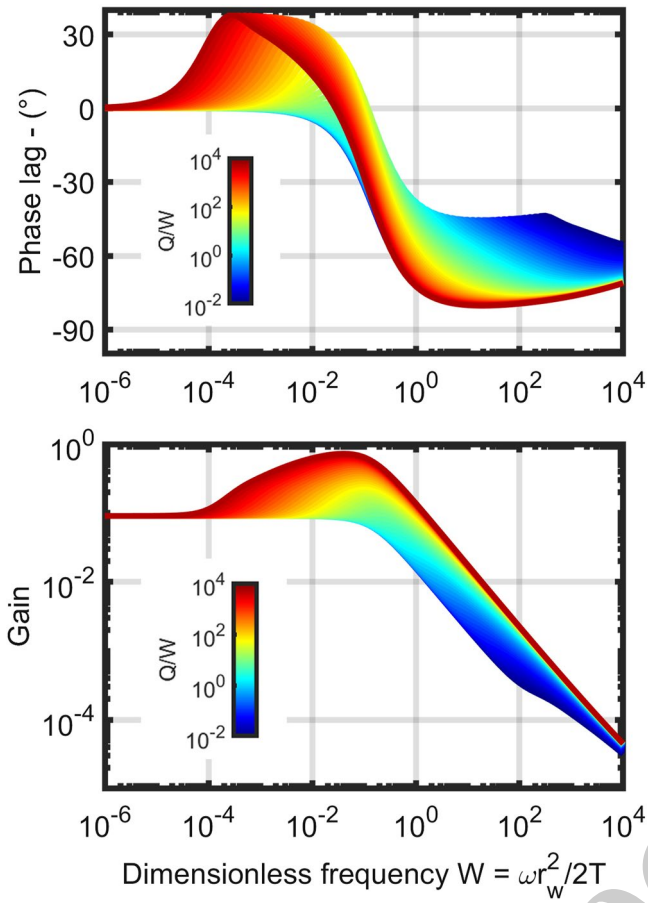

Figure 16. Chart of normalized Earth tide response $\frac{\rho g h_w}{B K_u \varepsilon}$ plotted in the same conditions as in (Sun et al., 2020, Figure 1). $S' = 10^{-5}$, $S = 10^{-6}$, $B' K'_u = 0$.

5.3. Impact of Oceanic Tide

Oceanic tide is intuitively a good candidate given the proximity to the ocean (2 km away). Yet several arguments show its contribution is negligible when compared with that of earth tide. Firstly, it has been showed that Martinique andesitic aquifers are compartmentalized (Vittecoq et al., 2015), such that no diffusion of oceanic pressure is possible. This geological consideration is striking when comparing different types of aquifers, all situated on the west coast of Martinique. Those in highly transmissive pyroclastic flows made of ashes are strongly coupled to the sea, as their spectrum show (Figure S2a in Supporting Information S1), the peak at the K1 frequency is higher than the one at the M2 frequency. On the contrary, all those in fractured andesite show the same pattern in their spectrum (Figure S2b in Supporting Information S1) with low or no peaks at the diurnal frequencies (O1, K1), and a higher peak at the M2 frequency. It leaves a mechanical transmission of the load the only possible process. Such a mechanical transmission would act on the aquifer similarly as earth tide. Analyzing the remaining piezometric signal after barometric influence is removed showed that oceanic tide signal could not explain the observed amplitudes and its effect is at least an order of magnitude lower than that of earth tide. Given that earth tide could already be treated as a small correction to the barometric effect (the S2 frequency is dominated by barometric contributions such that considering earth tide only changes the barometric phase lag by around 2°), we conclude that our results are unsensitive to oceanic loads and we neglect the correction linked to oceanic loads which effect are below our measurement uncertainty.

5.4. Comparison With Existing Models

Sun et al. (2020) proposed a review of the most important tidal response models, including (Hsieh et al., 1987; Rojstaczer, 1988; Wang et al., 2018). Figure 16 presents the transfer function calculated in the same context. As can be seen by comparing to Sun's charts, our model is closest to Rojstaczer (1988), who identified four imbalances in his introduction, between Earth surface, water table, confining layer, the aquifer and the well. He focused on the imbalance between the water table and the confining layer, neglecting the imbalance between the confining layer and the aquifer by setting $\gamma = \gamma'$, (or equivalently $BK_u = B'K'_u$, if he had dealt with earth tidal strain). As already pointed in (Odling et al., 2015), his model was imprecise in the low frequency regime, that's why our model predicts 0° phase lag when $\omega \to 0$, while Rojstaczer's tends to +45°. We did not consider the imbalance at the water table because our two-layer aquifer is confined. On the contrary, we focus on the flow between the two layers constituting the aquifer: the fractured andesite layer and the altered andesite layer (Figures 2 and 5). Because of that, the most relevant model to compare to is from Brodsky and Prejean (2005), which studied the exchange of pressure between a fault layer where permeability was assumed high (our main aquifer layer with $W \ll 1$), and a host rock layer (similar to our aquitard layer). The main difference lies in the boundary conditions, since they derived the model in the restrictive case $b' \to +\infty$, in which our model coincide. In addition to the geometry change, we coupled this generalized exchange model to the classical Hsieh et al. (1987) one to take into account the borehole storage effect. Relatively to Rojstaczer's, the response changes significantly: the positive phase lag induced by vertical leakage, and especially the low frequency behavior is totally different: Rojstaczer (1988) predicts more attenuation with lower frequency, and a phase lag converging to −45°, while we converge toward 0° of phase lag and a fixed value of attenuation, which depends on the poroelastic parameters and the storativities. We also showed that the imbalance between the two layers can actually strongly influence the response. Depending on the relative value of poroelastic parameters (Table 1) the flow direction changes and thus the sign of the response in absence of borehole storage. Its effect is particularly visible in our context where storage is higher in the top layer, a more porous layer, than in the bottom layer made of fractured andesite.

Our model has a theoretical range of attainable phase lag between −135° and +45°, while previous model (Rojstaczer, 1988; C.-Y. Wang et al., 2018) were limited to −90°. With the borehole storage effect, like previously,

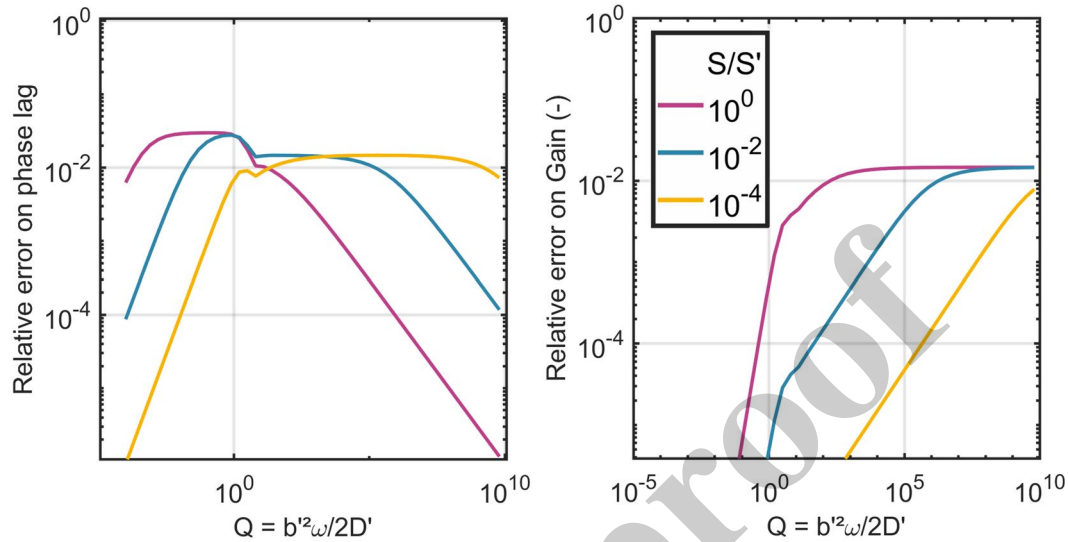

Figure 17. Relative error on phase lag (left) and amplitude gain (right) between the responses at the two frequencies M2 and S2.

we can reach the interval 0 to −90° (reaching −90° solely with borehole storage effect is actually unrealistic since it requires that S→0, Hsieh's original model chart stopped around −80°). With the exchange between the layers, we can reach −45° to +45° for both sources. Adding up all that we obtain the theoretical range of −135° to +45°. Yet we should remember that with phase lags comes attenuation so it is unrealistic to observe good quality signals with a phase lag of −135° (at least in the field case of Martinique where instruments have a mm resolution and where shallow aquifers elastic coefficients (like bulk moduli) are relatively low. A more realistic range of observation of phase lags in confined aquifers therefore seems −100° to +45°.

5.5. Validity of Our Hypotheses and Uncertainty Assessment

A first hypothesis we made was that the response varied slowly with frequency, so that we could assume the response was the same at M2 and S2 frequencies (1.93 and 2 cpd). In our range of parameters, the maximum absolute difference in response induced by a similar frequency difference (3.5%) was inferior to 0.17° for phase lag and 0.4% for gain, which is far below our measurement uncertainty, which is 1.9% for the gain and 1.6° for phase lag (Duvall, 1927). The results in term of relative errors are plotted on Figure 17. Both relative errors are below 3% on the full range of parameters. Another hypothesis we made was that the flow in the top layer was vertical. The top layer of altered andesite in a clay matrix is opened to the well, contrary to our conceptual model, in which the top layer was considered isolated from the well. Because the transmissivity of the top layer is so low compared to that of the bottom layer, the horizontal flow from that layer is considered negligible with respect to the horizontal flow from the bottom layer. Yet even if it is far less transmissive compared to the bottom layer, it is open to the well. What we implicitly did was neglecting the horizontal flow coming from the top layer. To assess this hypothesis we can apply the (Hsieh et al., 1987) model to the top layer and look at the resulting signal. For that we suppose that the horizontal diffusivity in the top layer is the same as its vertical diffusivity and look at the worst case (the highest estimated diffusivity and storativity). We obtain an estimated transmissivity of $10^{-7} m^2/s$, which yields a barometric signal with a gain of 3%, which is negligible with respect to our observed signal which gain was around 90%. Thus, the contribution of horizontal flow from the top layer is indeed negligible compared to that of the bottom one. Regarding the uncertainty on diffusivity and loading efficiency plotted on Figure 10, it mostly comes from the uncertainty on phase lag and measured gain (Figure 4). We propagated the uncertainty in the inversion of the model and plotted it in Figure S4 in Supporting Information S1, showing how uncertainty increases with increasing diffusivity.

6. Conclusion

In this study, we proposed a new conceptual model for a bi-layer aquifer and applied it to a volcanic aquifer from Martinique Island. It is able to predict positive phase lag for earth tide while the whole aquifer is confined, which is unprecedented in the literature. We performed a tidal analysis which enables to distinguish the contributions of the two identified sources of signal: solid-earth and atmospheric tides. The distinct response to these different sources yields useful information to understand the aquifer geometry and flow regime. Consequently, we were able to demonstrate that, starting from a general analytical model, we could use geological observations and the interpretation of tidal signals to constrain it down to a simpler site-specific model which could be explicitly inverted. These results were validated by several pumping tests spread across 14 years. We compared our model to existing ones, showing that keeping it as general as possible at first is an asset when trying to represent particular geometries.

The diffusion evolution we obtained yields important information on the phenomena that takes place. We induced a criterion for magnitude-distance selection of earthquakes that impact the aquifer. This criterion requires that dynamic strains from surface waves are responsible for the observed changes, since they decay as the square of the distance. This observation brings important information when trying to refine criteria for distinct phenomena, like water level changes, liquefaction, or, as set forth here, permeability changes. Secondly, we demonstrated that pumping tests are not innocent in the evolution of aquifer diffusivity, nor heavy tropical rainfall events, for which we proposed two possible mechanisms to explain the observed transient decreases in diffusivity, based on effective pressure and water viscosity change linked to colloids and particles.

Appendix A: Solution to the Diffusion Equation in the Top Layer

To solve for (13) with boundary conditions (14) and (15), we define the function

$$P = p' - \gamma' P_a \tag{A1}$$

We are looking for periodic solutions at a specific frequency ω. In complex notation, $\tilde{P} = Pe^{-i\omega t}$ is the solution of

$$\frac{\partial^2 \tilde{P}}{\partial z^2} = \frac{i\omega}{D'}\tilde{P} \tag{A2}$$

The boundary conditions are now:

$$\frac{\partial \tilde{P}}{\partial z}_{|z=b'} = 0 \tag{A3}$$

$$\tilde{P}(z=0) = \rho g \tilde{h}(r) - \gamma' \tilde{P}_a \tag{A4}$$

$\tilde{P}$ is of the form

$$\tilde{P} = P_1 \cosh\left(\sqrt{\frac{i\omega}{D'}}z\right) + P_2 \sinh\left(\sqrt{\frac{i\omega}{D'}}z\right) \tag{A5}$$

where $\sqrt{i} = \frac{1+i}{\sqrt{2}}$. $(A-4)$ yields that $P_1 = \rho g \tilde{h}(r) - \gamma' P_{a,0}$, and $(A-3)$ that $P_2 = -P_1 \tanh\left(\sqrt{\frac{i\omega}{D'}}b'\right)$, thus

$$\tilde{P}(z) = \left(\rho g \tilde{h}(r) - \gamma' P_{a,0}\right)\left(\cosh\left(\sqrt{\frac{i\omega}{D'}}z\right) - \tanh\left(\sqrt{\frac{i\omega}{D'}}b'\right)\sinh\left(\sqrt{\frac{i\omega}{D'}}z\right)\right) \tag{A6}$$

which immediately yields (16).

Appendix B: Solution to the Diffusion Equation in the Bottom Layer, Adapted From Wang et al. (2018)

Starting from Equation (18)

$$T\left(\frac{\partial^2\tilde{h}}{\partial r^2}+\frac{1}{r}\frac{\partial\tilde{h}}{\partial r}\right)-\frac{K'}{b'}\left(\tilde{h}-\frac{\gamma'}{\rho g}\tilde{P}_a\right)(1+i)\sqrt{Q}\cdot\tanh((1+i)\sqrt{Q})=i\omega S\left(\tilde{h}-\frac{\gamma}{\rho g}\tilde{P}_a\right)$$

We first solve for the hydraulic head away from the well $h_\infty(t)$, which also follows Equation (18) yet does not depend on r:

$$-\frac{K'}{b'}\left(\tilde{h}_\infty-\frac{\gamma'}{\rho g}\tilde{P}_a\right)(1+i)\sqrt{Q}\cdot\tanh((1+i)\sqrt{Q})=i\omega S\left(\tilde{h}_\infty-\frac{\gamma}{\rho g}\tilde{P}_a\right) \tag{B1}$$

Rearranging the terms, it yields the response:

$$\frac{\rho g\tilde{h}_\infty}{\tilde{P}_a}=\left(\frac{\gamma'+\gamma\cdot\dfrac{i\omega Sb'}{K'(1+i)\sqrt{Q}}\dfrac{1}{\tanh((1+i)\sqrt{Q})}}{1+\dfrac{i\omega Sb'}{K'(1+i)\sqrt{Q}}\dfrac{1}{\tanh((1+i)\sqrt{Q})}}\right) \tag{B2}$$

Noticing that $\frac{i\omega b'}{K'(1+i)}=\frac{(1+i)Q}{S'}$, it becomes

$$\frac{\rho g\tilde{h}_\infty}{\tilde{P}_a}=\left(\frac{\gamma'+\gamma\cdot\dfrac{S}{S'}\dfrac{(1+i)\sqrt{Q}}{\tanh((1+i)\sqrt{Q})}}{1+\dfrac{S}{S'}\dfrac{(1+i)\sqrt{Q}}{\tanh((1+i)\sqrt{Q})}}\right) \tag{B3}$$

Now we may solve for the effect of the well on the hydraulic head defined as the opposite of drawdown:

$$\Delta h(r,t)=h(r,t)-h_\infty(t) \tag{B4}$$

Substituting $h(r,t)$ by $\Delta h(r,t)+h_\infty(t)$ in (10) and inserting $(B-1)$, we get rid of the source terms and obtain:

$$T\left(\frac{\partial^2\Delta\tilde{h}}{\partial r^2}+\frac{1}{r}\frac{\partial\Delta\tilde{h}}{\partial r}\right)-\frac{K'}{b'}\Delta\tilde{h}(1+i)\sqrt{Q}\cdot\tanh((1+i)\sqrt{Q})=i\omega S\Delta\tilde{h} \tag{B5}$$

With adapted boundary conditions

$$\Delta\tilde{h}(r=\infty)=0 \tag{B6}$$

$$\Delta\tilde{h}(r_w,t)=\tilde{h}_w-\tilde{h}_\infty+\frac{\tilde{P}_a}{\rho g} \tag{B7}$$

$$2\pi r_wT\frac{\partial\Delta\tilde{h}}{\partial r}_{|r=r_w}=i\omega\pi r_c^2\tilde{h}_w \tag{B8}$$

From here we can draw a parallel with (Wang et al., 2018, Equations 9–12), which are like $(B-5)$ to $(B-8)$ once $\frac{K'}{b'}(1+i)\sqrt{Q}\cdot\tanh((1+i)\sqrt{Q})$ is substituted to $\frac{K'}{b'}$ and $-\tilde{h}_\infty+\frac{\tilde{P}_a}{\rho g}$ to $\tilde{h}_\infty$.

Hence, we define

$$\beta=\left(\frac{K'}{Tb'}(1+i)\sqrt{Q}\cdot\tanh((1+i)\sqrt{Q})+\frac{i\omega S}{T}\right)^{\frac{1}{2}} \tag{B9}$$

And by analogy

$$\Delta\tilde{h}(r,t)=-\frac{i\omega r_c^2K_0(\beta r)}{2T\beta r_wK_1(\beta r_w)}\tilde{h}_w \tag{B10}$$

Where K_0 and K_1 are the modified Bessel functions of the second kind, respectively of the zeroth and first order. Finally, $(B-10)$ yields with $(B-7)$ and $(B-3)$

$$\tilde{h}_w = \frac{\tilde{P}_a}{\rho g} \cdot \frac{1}{\xi} \left(\frac{\gamma' - 1 + (\gamma - 1)\frac{S}{S'} \frac{(1+i)\sqrt{Q}}{\tanh((1+i)\sqrt{Q})}}{1 + \frac{S}{S'} \frac{(1+i)\sqrt{Q}}{\tanh((1+i)\sqrt{Q})}} \right) \tag{B11}$$

With

$$\xi = 1 + \left(\frac{r_c}{r_w} \right)^2 \frac{i\omega r_w}{2T\beta} \frac{K_0(\beta r_w)}{K_1(\beta r_w)} \tag{B12}$$

It is interesting to write these results as a function of adimensional parameters which were studied in the literature before, namely in (Hsieh et al., 1987; Rojstaczer, 1988). We thus define in addition to Q

$$W = \frac{r_w^2 \omega}{2T}; \quad c_r = \left(\frac{r_c}{r_w} \right)^2 \tag{B13}$$

And now

$$\xi = 1 + i \cdot c_r \frac{W}{\beta r_w} \frac{K_0(\beta r_w)}{K_1(\beta r_w)} \tag{B14}$$

$$\beta r_w = \sqrt{W} \left(\frac{(1+i)\tanh((1+i)\sqrt{Q})}{\sqrt{Q}} S' + 2iS \right)^{\frac{1}{2}} \tag{B15}$$

Appendix C: Analytical Solution of Equations 24 and 25

Starting back from Equation (24)

$$\frac{\rho g \tilde{h}_w}{\tilde{P}_a} = \frac{\gamma' - 1}{1 + \frac{S}{S'} \frac{(1+i)\sqrt{Q}}{\tanh((1+i)\sqrt{Q})}}$$

Provided $\sqrt{Q} > 10$, which ensures that $\tanh((1+i)\sqrt{Q}) = 1$, an analytical inversion can be performed. If we set ϕ and G to respectively be the barometric phase lag and gain plotted in Figures 4a–4c, we get

$$\phi = \arg\left(\frac{\rho g \tilde{h}_w}{-\tilde{P}_a} \right) = \arg\left(\frac{1 - \gamma'}{1 + \frac{S}{S'}(1+i)\sqrt{Q}} \right) \tag{C1}$$

$$\phi = \arg\left(1 + \frac{S}{S'}(1-i)\sqrt{Q} \right) \tag{C2}$$

Thus,

$$\tan(\phi) = -\frac{\frac{S}{S'}\sqrt{Q}}{1 + \frac{S}{S'}\sqrt{Q}} \tag{C3}$$

And finally:

$$\sqrt{Q} = \frac{S'}{S} \cdot \frac{-\tan(\phi)}{1 + \tan(\phi)} \tag{C4}$$

Once Q is known, the gain immediately yields γ' :

$$\gamma' = 1 - G * \left\| 1 + \frac{S}{S'}(1+i)\sqrt{Q} \right\| \tag{C5}$$

Following the same process for earth tide, starting from Equation (25):

$$\frac{\rho g \tilde{h}_w}{\tilde{\varepsilon}} = \frac{BK_u \cdot \left(\frac{S}{S'}(1+i)\sqrt{Q} \right)}{1 + \frac{S}{S'}(1+i)\sqrt{Q}}$$

If we set ϕ and G to respectively be the earth tide phase lag and gain plotted in Figures 4b–4d, we get

$$\phi = \arg\left(1 + i + 2\frac{S}{S'}\sqrt{Q}\right) \tag{C6}$$

$$\tan(\phi) = \frac{1}{1 + 2\frac{S}{S'}\sqrt{Q}} \tag{C7}$$

And finally

$$\sqrt{Q} = \frac{S'}{S} \cdot \frac{1 - \tan(\phi)}{2\tan(\phi)} \tag{C8}$$

$$BK_u = G \left\| \frac{\frac{1-i}{2} + \frac{S}{S'}\sqrt{Q}}{\frac{S}{S'}\sqrt{Q}} \right\| \tag{C9}$$

Data Availability Statement

Piezometric data are available here: https://ades.eaufrance.fr/Fiche/PtEau?Code=1177ZZ0177/PZ2. The borehole national reference is BSS002NPJJ (1177ZZ0177/PZ2). The barometric data have been purchased from the French meteorological agency (Météo-France) and are subject to a disclaimer of diffusion. Access to these barometric data is granted to any scientific project organized by a university or research institute as long as the activity is not for profit and results are submitted for publication. Request to access the data must be addressed here: https://donneespubliques.meteofrance.fr/?fond=contact&id_produit=93&commande=1. Station number is 97,209,004 and further information about it is available here: https://donneespubliques.meteofrance.fr/metadonnees_publiques/fiches/fiche_97209004.pdf. Theoretical tidal strain were computed thanks to the SPOTL program (Agnew, 2012).

Acknowledgments
This research project, HydroSeisme (2021–2023), was funded by ERC Persismo, led by Harsha S. Bhat (ENS), by the initiative Ecosphere Continentale et Cotière (EC2CO) of the Institut National des Sciences de l'Univers/Centre National de la Recherche Scientifique (INSU/CNRS), and from BRGM Sism'Eau Project (An internal M4 research program). We wish to thank Emile Gros from BRGM Martinique who participated to the pumping test campaign.

References

Acworth, R. I., Halloran, L. J. S., Rau, G. C., Cuthbert, M. O., & Bernardi, T. L. (2016). An objective frequency domain method for quantifying confined aquifer compressible storage using Earth and atmospheric tides. *Geophysical Research Letters*, *43*(22). https://doi.org/10.1002/2016GL071328

Agnew, D. C. (2012). *Spotl: Some programs for ocean-tide loading [SIO Technical Report]* (p. 30). Scripps Institution of Oceanography. Retrieved from http://escholarship.org/uc/item/954322pg

Agnew, D. C. (2015). 3.06—Earth tides. In G. Schubert (Ed.), *Treatise on geophysics* (2nd ed., pp. 151–178). Elsevier. https://doi.org/10.1016/B978-0-444-53802-4.00058-0

Aki, K., & Richards, P. G. (2002). *Quantitative seismology* (2nd ed.). University Science Books. Retrieved from www.uscibooks.com

Bailly, C., Fortin, J., Adelinet, M., & Hamon, Y. (2019). Upscaling of elastic properties in carbonates: A modeling approach based on a multiscale geophysical data set. *Journal of Geophysical Research: Solid Earth*, *124*(12), 13021–13038. https://doi.org/10.1029/2019JB018391

Barbosa, N. D., Hunziker, J., Lissa, S., Saenger, E. H., & Lupi, M. (2019). Fracture unclogging: A numerical study of seismically induced viscous shear stresses in fluid-saturated fractured rocks. *Journal of Geophysical Research*, *23*(11), 11705–11727. https://doi.org/10.1029/2019jb017984

Barker, J. A. (1988). A generalized radial flow model for hydraulic tests in fractured rock. *Water Resources Research*, *24*(10), 1796–1804. https://doi.org/10.1029/WR024i010p01796

Boeut, S., Fujii, Y., Kodama, J.-I., Fukuda, D., Dassanayake, A., & Alam, B. A. K. M. (2020). Laboratory investigation on the permeability variation of fractured inada granite by multiple transient axial stress disturbances. *Pure and Applied Geophysics*, *177*(11), 5385–5396. https://doi.org/10.1007/s00024-020-02565-2

Brajanovski, M., Gurevich, B., & Schoenberg, M. (2005). A model for *P*-wave attenuation and dispersion in a porous medium permeated by aligned fractures. *Geophysical Journal International*, *163*(1), 372–384. https://doi.org/10.1111/j.1365-246X.2005.02722.x

Brodsky, E. E., Roeloffs, E., Woodcock, D., Gall, I., & Manga, M. (2003). A mechanism for sustained groundwater pressure changes induced by distant earthquakes. *Journal of Geophysical Research*, *108*(B8), 10. https://doi.org/10.1029/2002JB002321

Brodsky, E. E., & Prejean, S. G. (2005). New constraints on mechanisms of remotely triggered seismicity at long valley caldera: Triggering CONSTRAINTS. *Journal of Geophysical Research*, *110*(B4). https://doi.org/10.1029/2004JB003211

Candela, T., Brodsky, E. E., Marone, C., & Elsworth, D. (2014). Laboratory evidence for particle mobilization as a mechanism for permeability enhancement via dynamic stressing. *Earth and Planetary Science Letters*, *13*, 279–291. https://doi.org/10.1016/j.epsl.2014.02.025

Carlson, F., & Randall, J. (2012). Mlu: A windows application for the analysis of aquifer tests and the design of well fields in layered systems. *Groundwater*, *50*(4), 504–510. https://doi.org/10.1111/j.1745-6584.2012.00945.x

DeMets, C., Jansma, P. E., Matti, G. S., Dixon, T. H., Farina, F., Bilham, R., et al. (2000). GPS geodetic constraints on Caribbean-North America plate motion. *Geophysical Research Letter*, *27*(3), 437–440. https://doi.org/10.1029/1999GL005436

Doan, M.-L., Brodsky, E. E., Prioul, R., & Signer, C. (2008). *Tidal analysis of borehole pressure: A tutorial* (p. 60). University of California.

Duvall, C. R. (1927). Memorandum on the uncertainty in the amplitudes and phase-angles of Fourier terms. *Terrestrial Magnitude Atmosphere Electrical*, *32*(2), 65–68. https://doi.org/10.1029/TE032i002p00065

Elkhoury, J. E., Brodsky, E. E., & Agnew, D. C. (2006). Seismic waves increase permeability (Vol. *441*, p. 4). https://doi.org/10.1038/nature04798

Elkhoury, J. E., Niemeijer, A., Brodsky, E. E., & Marone, C. (2011). Laboratory observations of permeability enhancement by fluid pressure oscillation of in situ fractured rock. *Journal of Geophysical Research*, *116*(B2), B02311. https://doi.org/10.1029/2010JB007759

Gallagher, A., Fortin, J., & Borgomano, J. (2022). Seismic dispersion and attenuation in fractured fluid-saturated porous rocks: An experimental study with an analytic and computational comparison. *Rock Mechanics and Rock Engineering*, *55*(7), 4423–4440. https://doi.org/10.1007/s00603-022-02875-y

Gassman, F. (1951). Uber die Elastizitat Poroser Medien. *Vier Der Natur Gesellschaft in Zurich*, 1–23.

Hantush, M. S., & Jacob, C. E. (1955). Non-steady radial flow in an infinite leaky aquifer. *Eos, Transactions American Geophysical Union*, *36*(1), 95–100. https://doi.org/10.1029/tr036i001p00095

He, A., Singh, R. P., Sun, Z., Ye, Q., & Zhao, G. (2016). Comparison of regression methods to compute atmospheric pressure and Earth tidal coefficients in water level associated with Wenchuan Earthquake of 12 May 2008. *Pure and Applied Geophysics*, *173*(7), 18–2294. https://doi.org/10.1007/s00024-016-1310-3

Hsieh, P. A., Bredehoeft, J. D., & Farr, J. M. (1987). Determination of aquifer transmissivity from Earth tide analysis. *Water Resources Research*, *23*(10), 10–1832. https://doi.org/10.1029/WR023i010p01824

Ingebritsen, S. E., & Manga, M. (2019). Earthquake hydrogeology (Vol. *13*).

Kachanov, M., & Abedian, B. (2015). On the isotropic and anisotropic viscosity of suspensions containing particles of diverse shapes and orientations. *International Journal of Engineering Science*, *94*, 71–85. https://doi.org/10.1016/j.ijengsci.2015.05.003

Larochelle, S., Chanard, K., Fleitout, L., Fortin, J., Gualandi, A., Longuevergne, L., et al. (2022). Understanding the geodetic signature of large aquifer systems: Example of the Ozark plateaus in central United States. *Journal of Geophysical Research: Solid Earth*, *127*(3). https://doi.org/10.1029/2021JB023097

Leclerc, F. (2014). *Déformation active permanente induite par le méga-chevauchement dans l'arc antillais: Apport des complexes récifaux quaternaires*. IPGP.

Maas, C. (1987). Groundwater flow to a well in a layered porous medium: 2. Nonsteady multiple-aquifer flow. *Water Resources Research*, *23*(8), 1683–1688. https://doi.org/10.1029/WR023i008p01683

Manga, M. (2001). Origin of postseismic streamflow changes inferred from baseflow recession and magnitude-distance relations. *Geophysical Research Letters*, *28*(10), 2133–2136. https://doi.org/10.1029/2000GL012481

Manga, M., Beresnev, I., Brodsky, E. E., Elkhoury, J. E., Elsworth, D., Ingebritsen, S. E., et al. (2012). Changes in permeability caused by transient stresses: Field observations, experiments, and mechanisms: Dynamic permeability. *Reviews of Geophysics*, *50*(2). https://doi.org/10.1029/2011RG000382

Manga, M., & Wang, C.-Y. (2015). Earthquake hydrology. In *Treatise on geophysics* (pp. 305–328). Elsevier. https://doi.org/10.1016/B978-0-444-53802-4.00082-8

McMillan, T. C., Rau, G. C., Timms, W. A., & Andersen, M. S. (2019). Utilizing the impact of Earth and atmospheric tides on groundwater systems: A review reveals the future potential. *Reviews of Geophysics*, *57*(2), 281–315. https://doi.org/10.1029/2018RG000630

Méité, D., Rafini, S., Chesnaux, R., & Ferroud, A. (2022). Review of petroleum and hydrogeology equations for characterizing the pressure front diffusion during pumping tests. *Geosciences*, *12*(5), 201. https://doi.org/10.3390/geosciences12050201

Météo France. (2008). Bulletin climatologique mensuel Martinique—Octobre 2008. Retrieved from https://donneespubliques.meteofrance.fr/

Montgomery, D. R., & Manga, M. (2003). Streamflow and water well responses to earthquakes. *Science*, *300*(5628), 2047–2049. https://doi.org/10.1126/science.1082980

Muir-Wood, R., & King, G. C. P. (1993). Hydrological signatures of earthquake strain. *Journal of Geophysical Research*, *98*(B12), 22035–22068. https://doi.org/10.1029/93JB02219

Neuman, S. P. (1972). Theory of flow in unconfined aquifers considering delayed response of the water table. *Water Resources Research*, *8*(4), 1031–1045. https://doi.org/10.1029/WR008i004p01031

Odling, N. E., Perulero Serrano, R., Hussein, M. E. A., Riva, M., & Guadagnini, A. (2015). Detecting the vulnerability of groundwater in semi-confined aquifers using barometric response functions. *Journal of Hydrology*, *520*, 143–156. https://doi.org/10.1016/j.jhydrol.2014.11.016

Rau, G. C., McMillan, T. C., Andersen, M. S., & Timms, W. A. (2022). In situ estimation of subsurface hydro-geomechanical properties using the groundwater response to semi-diurnal Earth and atmospheric tides. *Hydrology and Earth System Sciences*, *26*(16), 4301–4321. https://doi.org/10.5194/hess-26-4301-2022

Roeloffs, E. (1996). Poroelastic techniques in the study of earthquake-related hydrologic phenomena. *Advances in Geophysics*, *37*, 135–195. https://doi.org/10.1016/S0065-2687(08)60270-8

Roeloffs, E., Sneed, M., Galloway, D. L., Sorey, M. L., Farrar, C. D., Howle, J. F., & Hughes, J. (2003). Water-level changes induced by local and distant earthquakes at Long Valley caldera, California. *Journal of Volcanology and Geothermal Research*, *127*(3–4), 269–303. https://doi.org/10.1016/S0377-0273(03)00173-2

Roeloffs, E. A. (1998). Persistent water level changes in a well near Parkfield, California, due to local and distant earthquakes. *Journal of Geophysical Research*, *103*(B1), 869–889. https://doi.org/10.1029/97JB02335

Rojstaczer, S. (1988). Determination of fluid flow properties from the response of water levels in wells to atmospheric loading. *Water Resources Research*, *24*(11), 1927–1938. https://doi.org/10.1029/WR024i011p01927

Rojstaczer, S., & Agnew, D. C. (1989). The influence of formation material properties on the response of water levels in wells to Earth tides and atmospheric loading. *Journal of Geophysical Research*, *94*(B9), 12403. https://doi.org/10.1029/JB094iB09p12403

Rojstaczer, S., & Riley, F. S. (1990). Response of the water level in a well to Earth tides and atmospheric loading under unconfined conditions. *Water Resources Research*, *26*(8), 1803–1817. https://doi.org/10.1029/WR026i008p01803

Rojstaczer, S., Wolft, S., & Micheli, R. (1995). Permeability enhancement in the shallow crust as a cause of earthquake-induced hydrological changes. *Nature*, *373*(6511), 3239. https://doi.org/10.1038/373237a0

Shi, Y., Liao, X., Zhang, D., & Liu, C. (2019). Seismic waves could decrease the permeability of the shallow crust. *Geophysical Research Letters*, *46*(12), 6371–6377. https://doi.org/10.1029/2019GL081974

Sun, X., Shi, Z., & Xiang, Y. (2020). Frequency dependence of in situ transmissivity estimation of well-aquifer systems from periodic loadings. *Water Resources Research*, *56*(11). https://doi.org/10.1029/2020WR027536

Theis, C. V. (1935). The relation between the lowering of the Piezometric surface and the rate and duration of discharge of a well using ground-water storage. *Transactions - American Geophysical Union*, *16*, 519–524. https://doi.org/10.1029/tr016i002p00519

Valois, R., Rau, G. C., Vouillamoz, J.-M., & Derode, B. (2022). Estimating hydraulic properties of the shallow subsurface using the groundwater response to Earth and atmospheric tides: A comparison with pumping tests. *Water Resources Research*, *36*(5). https://doi.org/10.1029/2021WR031666

Vittecoq, B., & Brugeron, A. (2008). *Recherche d'eau souterraine à Schoelcher – Fond Lahaye (RP-55728-FR*. BRGM. 242. Retrieved from http://ficheinfoterre.brgm.fr/document/RP-55728-FR

Vittecoq, B., Fortin, J., Maury, J., & Violette, S. (2020). Earthquakes and extreme rainfall induce long term permeability enhancement of volcanic island hydrogeological systems. *Scientific Reports*, *10*(1), 20231. https://doi.org/10.1038/s41598-020-76954-x

Vittecoq, B., Reninger, P.-A., Lacquement, F., Martelet, G., & Violette, S. (2019). Hydrogeological conceptual model of andesitic watersheds revealed by high-resolution heliborne geophysics. *Hydrology and Earth System Sciences*, *23*(5), 2321–2338. https://doi.org/10.5194/hess-23-2321-2019

Vittecoq, B., Reninger, P. A., Violette, S., Martelet, G., Dewandel, B., & Audru, J. C. (2015). Heterogeneity of hydrodynamic properties and groundwater circulation of a coastal andesitic volcanic aquifer controlled by tectonic induced faults and rock fracturing – Martinique island (Lesser Antilles – FWI). *Journal of Hydrology*, *529*, 1041–1059. https://doi.org/10.1016/j.jhydrol.2015.09.022

Wang, C., Liao, X., Wang, L., Wang, C., & Manga, M. (2016). Large earthquakes create vertical permeability by breaching aquitards. *Water Resources Research*, *52*(8), 5923–5937. https://doi.org/10.1002/2016WR018893

Wang, C.-Y., Doan, M.-L., Xue, L., & Barbour, A. J. (2018). Tidal response of groundwater in a leaky aquifer—Application to Oklahoma. *Water Resources Research*, *15*(10), 8019–8033. https://doi.org/10.1029/2018wr022793

Wang, C.-Y., & Manga, M. (2010). Hydrologic responses to earthquakes and a general metric. *Geofluids*. https://doi.org/10.1111/j.1468-8123.2009.00270.x

Wang, C.-Y., & Manga, M. (2015). New streams and springs after the 2014 Mw6.0 south Napa earthquake. *Nature Communications*, *6*(1), 7597. https://doi.org/10.1038/ncomms8597

Wang, C.-Y., Wang, C.-H., & Kuo, C.-H. (2004). Temporal change in groundwater level following the 1999 (Mw = 7.5) Chi-Chi earthquake, Taiwan. *Geofluids*, *4*(3), 210–220. https://doi.org/10.1111/j.1468-8123.2004.00082.x

Wang, H., Xin, J., Zheng, X., Li, M., Fang, Y., & Zheng, T. (2020). Clogging evolution in porous media under the coexistence of suspended particles and bacteria: Insights into the mechanisms and implications for groundwater recharge. *Journal of Hydrology*, *582*, 124554. https://doi.org/10.1016/j.jhydrol.2020.124554

Wang, H. F. (2000). *Theory of linear poroelasticity with applications to geomechanics and hydrogeology*. Princeton University Press.

Warren, J. E., & Root, P. J. (1963). The behavior of naturally fractured reservoirs. *Society of Petroleum Engineers Journal*, *3*(03), 245–255. https://doi.org/10.2118/426-PA

Westercamp, D., Pelletier, B., Thibault, P. M., & Traineau, H. (1990). *Carte géologique de la Martinique au 1/50000ème*. Editions BRGM. Retrieved from http://infoterre.brgm.fr/formulaire/telechargement-cartes-geologiques-drom

Xiang, Y., Sun, X., & Gao, X. (2019). Different coseismic groundwater level changes in two adjacent wells in a fault-intersected aquifer system. *Journal of Hydrology*, *578*, 124123. https://doi.org/10.1016/j.jhydrol.2019.124123

Xue, L., Li, H.-B., Brodsky, E. E., Xu, Z.-Q., Kano, Y., Wang, H., et al. (2013). *Continuous permeability measurements record healing inside the Wenchuan Earthquake fault zone*, *340*, 6. https://doi.org/10.1126/science.1237237

Yan, R., Woith, H., & Wang, R. (2014). Groundwater level changes induced by the 2011 Tohoku earthquake in China mainland (Vol. *16*).

Zhang, H., Shi, Z., Wang, G., Sun, X., Yan, R., & Liu, C. (2019). Large earthquake reshapes the groundwater flow system: Insight from the water-level response to Earth tides and atmospheric pressure in a deep well. *Water Resources Research*, *13*. https://doi.org/10.1029/2018WR024608

Zhang, S., Shi, Z., & Wang, G. (2019). Comparison of aquifer parameters inferred from water level changes induced by slug test, Earth tide and earthquake – A case study in the three Gorges area. *Journal of Hydrology*, *10*, 124169. https://doi.org/10.1016/j.jhydrol.2019.124169